

Ca²⁺ channel and active zone protein abundance intersects with input-specific synapse organization to shape functional synaptic diversity

Audrey T Medeiros¹, Scott J Gratz^{2*}, Ambar Delgado², Jason T Ritt^{2,3},
Kate M O'Connor-Giles^{1,2,3*}

¹Neuroscience Graduate Training Program, Brown University, Providence, United States; ²Department of Neuroscience, Brown University, Providence, United States; ³Carney Institute for Brain Science, Brown University, Providence, United States

Abstract Synaptic heterogeneity is a hallmark of nervous systems that enables complex and adaptable communication in neural circuits. To understand circuit function, it is thus critical to determine the factors that contribute to the functional diversity of synapses. We investigated the contributions of voltage-gated calcium channel (VGCC) abundance, spatial organization, and subunit composition to synapse diversity among and between synapses formed by two closely related *Drosophila* glutamatergic motor neurons with distinct neurotransmitter release probabilities (P_r). Surprisingly, VGCC levels are highly predictive of heterogeneous P_r among individual synapses of either low- or high- P_r inputs, but not between inputs. We find that the same number of VGCCs are more densely organized at high- P_r synapses, consistent with tighter VGCC-synaptic vesicle coupling. We generated endogenously tagged lines to investigate VGCC subunits in vivo and found that the $\alpha 2\delta$ -3 subunit Straightjacket along with the CAST/ELKS active zone (AZ) protein Bruchpilot, both key regulators of VGCCs, are less abundant at high- P_r inputs, yet positively correlate with P_r among synapses formed by either input. Consistently, both Straightjacket and Bruchpilot levels are dynamically increased across AZs of both inputs when neurotransmitter release is potentiated to maintain stable communication following glutamate receptor inhibition. Together, these findings suggest a model in which VGCC and AZ protein abundance intersects with input-specific spatial and molecular organization to shape the functional diversity of synapses.

eLife assessment

Calcium channels are key regulators of synaptic strength and plasticity. The authors generate new endogenous tags of the *Drosophila* channel Cac as well as auxiliary subunits to investigate distinct calcium channel functions at the fly NMJ, Is and Ib. They demonstrate functions for voltage-gated calcium channel subunits in promoting synaptic strength, diversity, and plasticity with a series of **convincing** analyses. The work is **important** and has broad implications. In addition, the newly developed tools should be quite beneficial for fly biologists.

Introduction

The broad and complex functions of neural circuits depend on diverse neuronal subtypes communicating through synapses with distinct properties. Thus, understanding how synaptic diversity is established is critical for understanding neural circuit function. Neurotransmission occurs at specialized

*For correspondence:

scott_gratz@brown.edu (SJG);
kate_oconnor-giles@brown.edu
(KMO'C-G)

Competing interest: The authors declare that no competing interests exist.

Funding: See page 18

Preprint posted

10 April 2023

Sent for Review

02 May 2023

Reviewed preprint posted

17 July 2023

Reviewed preprint revised

18 July 2024

Version of Record published

18 September 2024

Reviewing Editor: Hugo J Bellen, Baylor College of Medicine, United States

© Copyright Medeiros et al. This article is distributed under the terms of the [Creative Commons Attribution License](https://creativecommons.org/licenses/by/4.0/), which permits unrestricted use and redistribution provided that the original author and source are credited.

membranes called active zones (AZs) where action potentials drive the opening of voltage-gated Ca^{2+} channels (VGCCs) to trigger Ca^{2+} -dependent synaptic vesicle (SV) fusion and neurotransmitter release. Neurotransmitter release properties are determined locally at individual synapses and vary considerably between neuronal subtypes and within homogeneous populations of neurons (Ariel et al., 2012; Atwood and Karunanithi, 2002; Branco and Staras, 2009; Hatt and Smith, 1976). In fact, functional imaging studies in *Drosophila* demonstrate that even single neurons forming synapses with the same postsynaptic partner display heterogeneous synaptic strength among individual AZs (Guerrero et al., 2005; Melom et al., 2013; Peled and Isacoff, 2011).

Presynaptic strength is defined as the likelihood of neurotransmitter release following an action potential (probability of release, P_r). This probabilistic process is determined by the number of functional SV release sites and their individual probability of vesicle release. The probability of SV release is highly dependent on transient increases in intracellular Ca^{2+} levels at vesicular sensors. Accordingly, SV release sites and VGCCs are key substrates for generating diversity of synaptic function (Akbergenova et al., 2018; Aldahabi et al., 2022; Chen et al., 2015; Fedchyshyn and Wang, 2005; Fekete et al., 2019; Gratz et al., 2019; Holderith et al., 2012; Laghaei et al., 2018; Miki et al., 2017; Nakamura et al., 2015; Newman et al., 2022; Rebola et al., 2019; Reddy-Alla et al., 2017; Sauvola et al., 2021; Sheng et al., 2012). Numerous studies have demonstrated that VGCC abundance is highly correlated with P_r across species (Akbergenova et al., 2018; Gratz et al., 2019; Holderith et al., 2012; Miki et al., 2017; Nakamura et al., 2015; Sheng et al., 2012). Paradoxically, this is not always the case. For example, a recent study investigated two cerebellar synaptic subtypes, one high- P_r formed by inhibitory stellate cells and one low- P_r formed by excitatory granule cells, and found higher VGCC levels at low- P_r granule synapses (Rebola et al., 2019). Since VGCCs in closer proximity to release sites are expected to have a greater impact on vesicular release probability than those positioned farther away, the spatial coupling of VGCCs and SVs at AZs is a critical determinant of P_r (Chen et al., 2015; Eggermann et al., 2011; Fedchyshyn and Wang, 2005; Nakamura et al., 2015; Rebola et al., 2019). Indeed, at high- P_r stellate synapses, a 'perimeter release' AZ organization places VGCCs ~40 nm closer to SVs than at low- P_r granular synapses (Rebola et al., 2019). Another recent study investigated two functionally distinct connections formed by CA1 pyramidal cells (Aldahabi et al., 2022). While Ca^{2+} influx was higher at the high- P_r synapse, raising Ca^{2+} influx at the low- P_r synapse to match the high- P_r synapse did not equalize P_r .

To further investigate this paradox, we sought a system where we could investigate the relationship between VGCCs and P_r both within and between two closely related neurons that form synapses with distinct release probabilities. *Drosophila* muscles are innervated by two glutamatergic motor neurons, one tonic and one phasic, that form type Ib and type Is synapses, respectively. Type Ib synapses have relatively low P_r and facilitate, whereas type Is synapses have higher P_r and depress in response to high-frequency stimulation (Aponte-Santiago et al., 2020; Lnenicka and Keshishian, 2000). In this study, we investigated how VGCC abundance, spatial organization, and subunit composition contribute to synaptic heterogeneity at AZs of low- P_r type Ib and high- P_r type Is inputs to the same postsynaptic targets. We find that individual synapses formed by both low- and high- P_r inputs exhibit heterogeneous release properties that can be predicted by VGCC abundance alone. However, VGCC abundance does not correspond to differences in P_r between the two inputs. We identify underlying molecular and organizational differences that may alter the relationship between VGCC abundance and P_r at low- vs. high- P_r inputs. We further find that the homeostatic potentiation of neurotransmitter release triggered by glutamate receptor inhibition involves dynamic increases in VGCCs, the $\alpha 2\delta$ -3 subunit Straightjacket (Stj), and the AZ cytomatrix protein Bruchpilot (Brp) across AZs of both inputs. These findings provide insight into how VGCC and AZ protein abundance intersects with underlying molecular and organizational differences between inputs to contribute to greater synaptic diversity.

Results

VGCC levels predict P_r within, but not between, inputs

To investigate the relationship between VGCC levels and neurotransmitter release properties at functionally distinct synapses, we took advantage of the two motor neuron subtypes with low and high release probabilities that innervate most *Drosophila* muscles (Aponte-Santiago and Littleton, 2020; Kurdyak et al., 1994). These glutamatergic neuromuscular junctions (NMJs) contain hundreds of

individual synapses that are accessible to single AZ functional imaging using genetically encoded Ca^{2+} indicators.

In *Drosophila*, Cacophony (Cac) is the sole Ca_v2 pore-forming subunit and is the VGCC responsible for triggering synaptic transmission (Kawasaki et al., 2000; Macleod et al., 2006; Peng and Wu, 2007; Smith et al., 1996). To simultaneously monitor neurotransmitter release and VGCC levels, we swapped the N-terminal sfGFP tag in our well-characterized $\text{cac}^{\text{sfGFP-N}}$ line for a Td-Tomato tag ($\text{cac}^{\text{Td-Tomato-N}}$) and confirmed that the tag does not impair synaptic function (Figure 1—figure supplement 1; Figure 1A–F; Ghelani et al., 2023; Gratz et al., 2019). We then expressed postsynaptically targeted GCaMP6f (SynapGCaMP6f; Newman et al., 2017), which reports Ca^{2+} influx through glutamate receptors in response to neurotransmitter release, in $\text{cac}^{\text{Td-Tomato-N}}$ animals for a plus/minus readout. We and others have previously shown that Cac levels are highly predictive of P_r at individual type Ib AZs (Akbergenova et al., 2018; Gratz et al., 2019). To determine if VGCC levels are similarly predictive at high- P_r type Is AZs, we measured $\text{Cac}^{\text{Td-Tomato-N}}$ fluorescence intensity and monitored neurotransmitter release in response to 0.2 Hz stimulus at individual synapses. To enable direct comparisons between the two inputs, we simultaneously imaged type Ib and Is synapses at NMJ 6/7 (Figure 1A). We quantified the number of times a vesicle was released over 120 stimuli to determine single-synapse P_r . As has been previously reported, we found that type Is synapses exhibited significant heterogeneity and higher average P_r than type Ib synapses (Figure 1B and C; Lu et al., 2016; Newman et al., 2022). Consistent with their higher P_r , type Is connections contain relatively fewer low- P_r and more high- P_r AZs (Figure 1D). We next investigated the correlation between P_r and VGCC levels and found that at type Is inputs, single-AZ Cac intensity positively correlates with P_r (Figure 1E). We also observe a strong positive correlation between VGCC levels and P_r at type Ib inputs to the same muscles (Figure 1F), consistent with our and others' prior findings (Akbergenova et al., 2018; Gratz et al., 2019; Newman et al., 2022).

A simple prediction of the observation that VGCC levels correlate highly with P_r at individual AZs of both low- and high- P_r inputs is that Cac levels will be higher at synapses of type Is inputs than type Ib. We analyzed $\text{Cac}^{\text{sfGFP-N}}$ levels at individual type Ib and Is synapses and found that average Cac levels are the same at type Ib and Is AZs (Figure 1G and H). Cac levels are also similarly distributed across AZs of the two inputs (Figure 1I). Together, these findings indicate that the relationship between VGCC levels and P_r differs between the two inputs. Consistently, when we directly compare the best-fit lines for the relationship between Cac levels and P_r at type Ib and Is inputs from our correlative functional imaging data (Figure 1E and F), we find that the slopes are significantly different (Figure 1J). Across type Is AZs, a similar range of VGCC levels supports a higher range of release probabilities. Thus, VGCCs can predict P_r within synaptic subtypes, but not between AZs of different synaptic subtypes, providing a framework for understanding seemingly contradictory findings on the role of VGCCs in determining P_r .

VGCC clusters are more compact at AZs of high- P_r type Is inputs

Many differences between low- P_r type Ib and high- P_r type Is AZs have been described (Aponte-Santiago and Littleton, 2020; Aponte-Santiago et al., 2020; Atwood et al., 1993; He et al., 2023; Jetti et al., 2023; Kurdyak et al., 1994; Lu et al., 2016; Medeiros and O'Connor-Giles, 2023). Perhaps most notably, type Is AZs experience ~twofold greater Ca^{2+} influx than type Ib (He et al., 2023; Lu et al., 2016). While this alone could explain the estimated 3-fold greater P_r at type Is AZs and is certainly a key factor, several lines of evidence argue for additional contributors. A recent study using a botulinum transgene to isolate type Ib and Is synapses for electrophysiological analysis found that increasing external $[\text{Ca}^{2+}]$ from physiological levels (1.8 mM) to 3 mM or even 6 mM does not result in a 3-fold increase in EPSCs or quantal content at type Ib synapses and type Ib synapses continue to facilitate at 3 mM external $[\text{Ca}^{2+}]$ (He et al., 2023). Using this approach, they further found that type Ib synapses are more sensitive to the slow Ca^{2+} chelator EGTA, indicating looser VGCC-SV coupling.

We investigated the spatial distribution of VGCCs at type Ib and Is AZs using 3D dSTORM single-molecule localization microscopy (SMLM). An individual VGCC complex is estimated to be ~10 nm in diameter with the most common immunolabeling techniques adding significantly to their size and creating a linkage error of ~20 nm between the target molecule and fluorescent reporter (Früh et al., 2021; Liu et al., 2022; Thomas, 2000). For following VGCC dynamics using single-particle

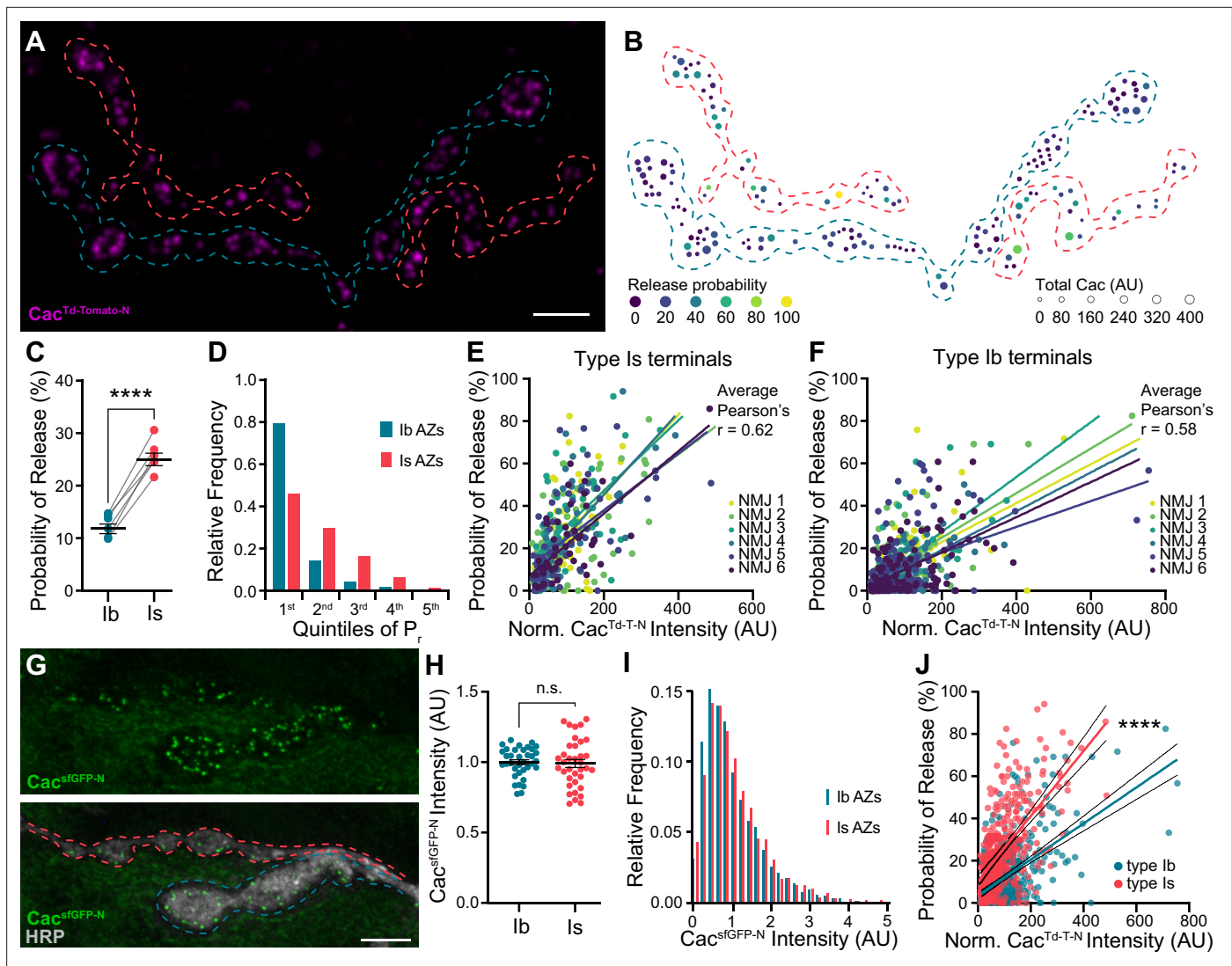


Figure 1. VGCC levels predict P_r within, but not between, inputs. **(A)** Representative confocal Z-projection of $Cac^{Td-Tomato-N}$ (magenta) with type Ib (blue) and type Is (red) terminals outlined. **(B)** AZ heat map of terminals in A with color indicating P_r , and size representing sum Cac intensity levels in arbitrary units (AU). **(C)** Average single-AZ probability of release at type Ib and Is terminals. $N=6$ animals, 6 NMJs. **(D)** Quintile distribution of single-AZ P_r , frequency at type Ib and Is inputs. **(E, F)** Correlation between normalized $Cac^{Td-Tomato-N}$ intensity and P_r at type Is and Ib AZs of the same 6 NMJs. Each dot represents a single AZ and each color corresponds to an individual NMJ with linear regression lines indicated for each. **(G)** Top, representative confocal Z-projection of $Cac^{sfGFP-N}$. Bottom, $Cac^{sfGFP-N}$ in green with HRP marking neuronal membranes in gray. Type Ib (blue) and type Is (red) terminals are outlined. **(H)** Quantification of $Cac^{sfGFP-N}$ AZ intensity at type Ib and Is terminals. Each data point represents the average normalized single AZ sum intensity for an individual NMJ. **(I)** Distribution of normalized $Cac^{sfGFP-N}$ intensity from single type Ib and Is AZs in H (X-axis cutoff at 5.0). **(J)** Comparison between normalized $Cac^{Td-Tomato-N}$ and P_r of type Ib and Is AZs combined from E-F with linear regression lines (blue and red, respectively) and 95% confidence intervals (black lines) indicated. All scale bars = 5 μm , all error bars indicate S.E.M, **** $p < 0.0001$; ns, not significant. N's, absolute values, and statistical information is detailed in **Supplementary file 1a**.

The online version of this article includes the following figure supplement(s) for figure 1:

Figure supplement 1. Electrophysiological validation of endogenously tagged cacophony lines.

(A-C) Representative traces of EJPs (top) and mEJPs (bottom) in control, $cac^{HaloTag-N}$, and $cac^{Td-Tomato-N}$. **(D-F)** Quantification of EJPs, mEJPs, and quantal content (QC). All error bars indicate S.E.M., ns, not significant.

tracking via photoactivation localization microscopy (sptPALM), we recently incorporated mEOS4b (*Paez-Segala et al., 2015*) at the same N-terminal site we previously used to endogenously tag Cac, achieving a linkage error of less than 5 nm (*Ghelani et al., 2023; Gratz et al., 2019*). To gain more flexibility in labeling Cac without adding to the linkage error, we swapped the mEOS tag for a similarly sized HaloTag ($cac^{HaloTag-N}$). $cac^{HaloTag-N}$ flies are fully viable, do not display significant defects in

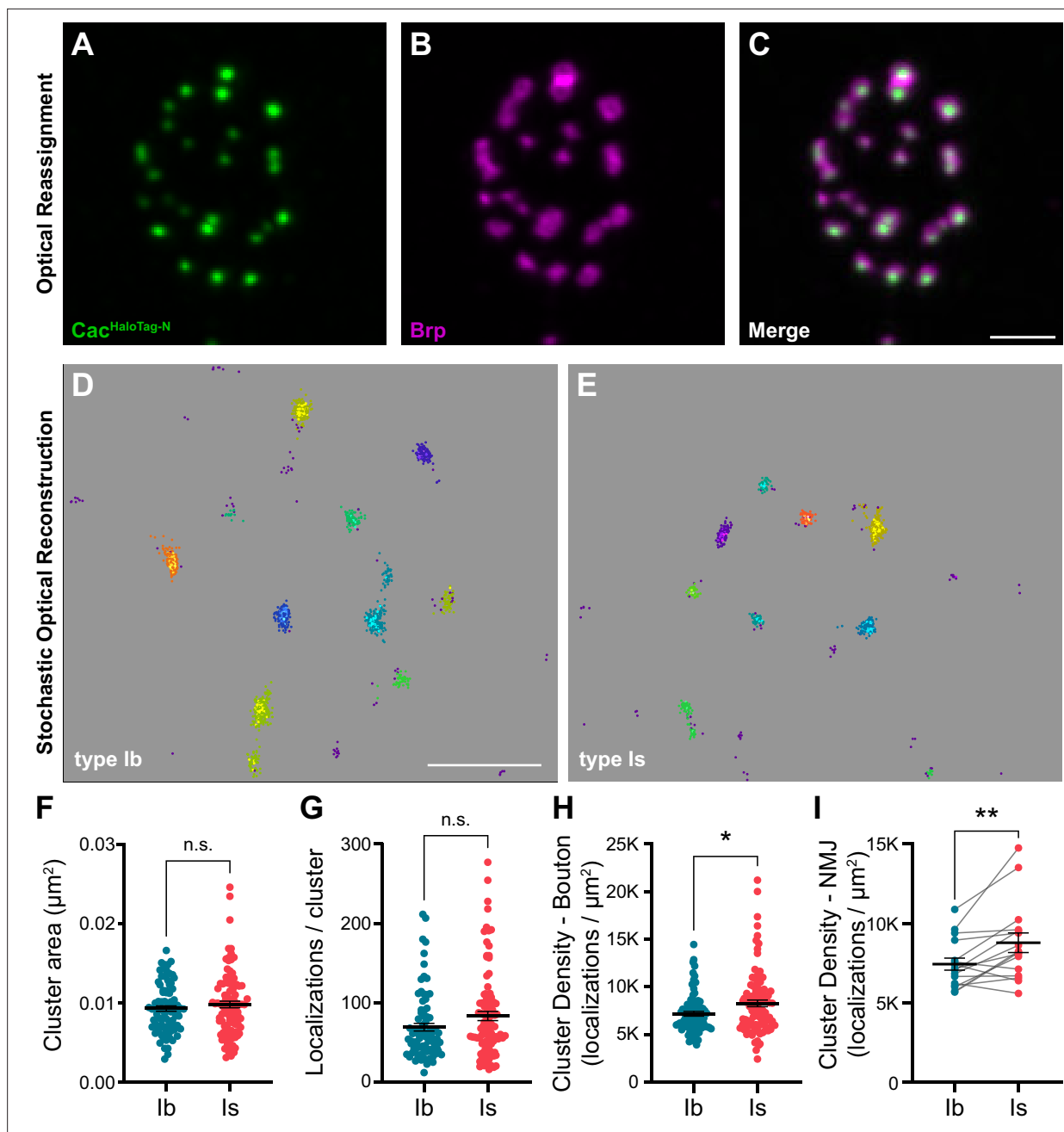


Figure 2. VGCC clusters are more compact at AZs of high-P, type Is inputs. (A–C) Representative SoRa Z-projection of $Cac^{HaloTag-N}$ (green), Brp (magenta), and merge. (D, E) Representative boutons of STORM $Cac^{HaloTag-N}$ clusters as identified by DBSCAN at type Ib and Is boutons as indicated. Each color represents an individual identified cluster with purple scattered dots identifying excluded background signal. (F–H) Analysis of STORM-acquired $Cac^{HaloTag-N}$ clusters where each data point represents the respective single-cluster measurement averaged over individual boutons. (F) Quantification of $Cac^{HaloTag-N}$ cluster area at type Ib and Is AZs. (G) Quantification of localizations per cluster at type Ib and Is boutons. (H) Calculated $Cac^{HaloTag-N}$ cluster density at type Ib and Is AZs. (I) Paired analysis of calculated AZ cluster density averaged over individual type Ib and Is inputs to the same muscle. All scale bars = 1 μm , all error bars indicate S.E.M. ** $p < 0.01$; * $p < 0.05$; ns, not significant. N's, absolute values, and statistical information is detailed in [Supplementary file 1a](#).

synaptic function, and exhibit normal Cac localization at AZs as observed in super-resolution optical reassignment images, where Brp is arranged in rings surrounding puncta of VGCCs ([Figure 1—figure supplement 1](#); [Figure 2A–C](#), [Ghelani et al., 2023](#)). HaloTag, which covalently binds synthetic ligands, is 3.3 nm in diameter ([Los et al., 2008](#); [Yazaki et al., 2020](#)), yielding a linkage error well under 5 nm. $cac^{HaloTag-N}$ larvae were stained with JaneliaFluor646 HaloTag ligand ([Grimm et al., 2015](#)) and

horseradish peroxidase (HRP) to distinguish between type Ib and Is branches and enable simultaneous imaging of the two inputs at a single NMJ. We then used density-based spatial clustering of applications with noise (DBSCAN) analysis to identify Cac clusters at type Ib and Is AZs (**Figure 2D and E; Ehmann et al., 2014**). We find that the average size of Cac^{HaloTag-N} clusters is similar at low- and high-P_r AZs (**Figure 2F**), with mean diameters of approximately 102 nm and 105 nm, respectively. This is similar to the Cac^{mE054b-N} type Ib cluster size observed by sptPALM imaging (**Ghelani et al., 2023**). In agreement with our confocal level data, the number of localizations per cluster was similar at low- and high-P_r AZs (**Figure 2G**). We then calculated the average Cac density per AZ and found that VGCCs are significantly more densely organized at high-P_r type Is AZs than low-P_r type Ib AZs (**Figure 2H, I**). Greater VGCC AZ density at type Is AZs is consistent with a recent SMLM study using antibodies to label Cac, indicating these results are robust to different labeling approaches (**Newman et al., 2022**). Together, these findings suggest that more compact organization of VGCCs increases their coupling to SVs and contributes to the steeper relationship between VGCC levels and P_r at high-P_r type Is AZs.

Differences in Bruchpilot levels and function at low- and high-P_r inputs

To understand how these nanoscale differences in VGCC organization might be established, we investigated the AZ scaffolding protein Brp. Brp/CAST/ELKS family proteins function as central organizers of both VGCCs and SV release sites at developing synapses (**Dai et al., 2006; Dong et al., 2018; Hallermann et al., 2010; Held et al., 2016; Kittel et al., 2006; Liu et al., 2014; McDonald et al., 2020; Radulovic et al., 2020**). Like Cac, Brp is more densely arranged at type Is AZs as measured through SMLM and stimulated emission depletion (STED) imaging studies (**He et al., 2023; Jetti et al., 2023; Mrestani et al., 2021**). We simultaneously imaged type Ib and Is inputs and found lower Brp levels at type Is AZs (**Figure 3A and B**). Since Cac levels are similar at AZs of the two inputs, lower Brp levels result in a significantly higher Cac:Brp ratio at type Is synapses, which we hypothesize promotes compact organization of VGCCs (**Figure 3C**). In contrast, we and others have previously shown that Brp levels positively correlate with P_r among AZs of low-P_r type Ib inputs (**Gratz et al., 2019; Muhammad et al., 2015; Newman et al., 2017; Peled et al., 2014; Reddy-Alla et al., 2017**). Consistently, Brp and Cac levels strongly correlate at type Ib AZs (**Gratz et al., 2019**) and we observe a similarly strong correlation across individual type Is AZs (**Figure 3D**). Thus, like VGCCs, Brp levels contribute in distinct ways to synaptic heterogeneity within vs. between low- and high-P_r inputs, likely due to differences in AZ organization between the two synaptic subtypes.

We next investigated the requirement for Brp in promoting VGCC accumulation at low- and high-P_r inputs by analyzing Cac^{sGFP-N} levels in *brp* null mutants (*brp*^{-/-}; **Figure 3E and F**). Cac^{sGFP-N} levels are diminished at both type Ib and Is AZs, demonstrating a conserved role for Brp in promoting Cac accumulation at both inputs (**Figure 3G**). The relative decrease in Cac levels at type Ib AZs is significantly greater than at type Is AZs, indicating a greater requirement for Brp in regulating VGCC levels at low-P_r type Ib synapses (**Figure 3H**). This suggests that an additional factor or factors function with or upstream of Brp to establish differences in Brp dependence at low- and high-P_r AZs.

Brp differentially regulates VGCC dynamics at low- and high-P_r synapses during presynaptic homeostatic potentiation

In response to acute or chronic inhibition of glutamate receptors at NMJs, *Drosophila* motor neurons homeostatically increase neurotransmitter release to maintain synaptic communication (**Davis and Müller, 2015; Frank, 2014; James et al., 2019**). Pharmacological inhibition of glutamate receptors with the wasp toxin Philanthotoxin-433 (PhTx) induces acute presynaptic homeostatic potentiation of release (PHP) within minutes (**Frank et al., 2006**). We and others have demonstrated that acute PHP involves rapid changes in VGCC and other AZ protein levels at type Ib AZs (**Böhme et al., 2019; Gratz et al., 2019; Weyhersmüller et al., 2011**). Recent studies have revealed significant differences in the induction of PHP at low- and high-P_r synaptic inputs under different conditions (**Genç and Davis, 2019; Newman et al., 2017; Sauvola et al., 2021**). PhTx induces acute PHP at both type Ib and Is synapses (**Genç and Davis, 2019**), but the molecular changes underlying PHP at high-P_r type Is AZs remain unknown. To compare the dynamic modulation of VGCCs at low- and high-P_r AZs, we treated *cac*^{sGFP-N} larvae with non-saturating concentrations of PhTx for 10 min, then quantified Cac and Brp levels at type Ib and Is AZs (**Figure 4A and B**). We observe a significant PhTx-induced increase in Brp and Cac^{sGFP-N} levels at type Is AZs similar to type Ib (**Figure 4C and D; Gratz et al., 2019**). Thus,

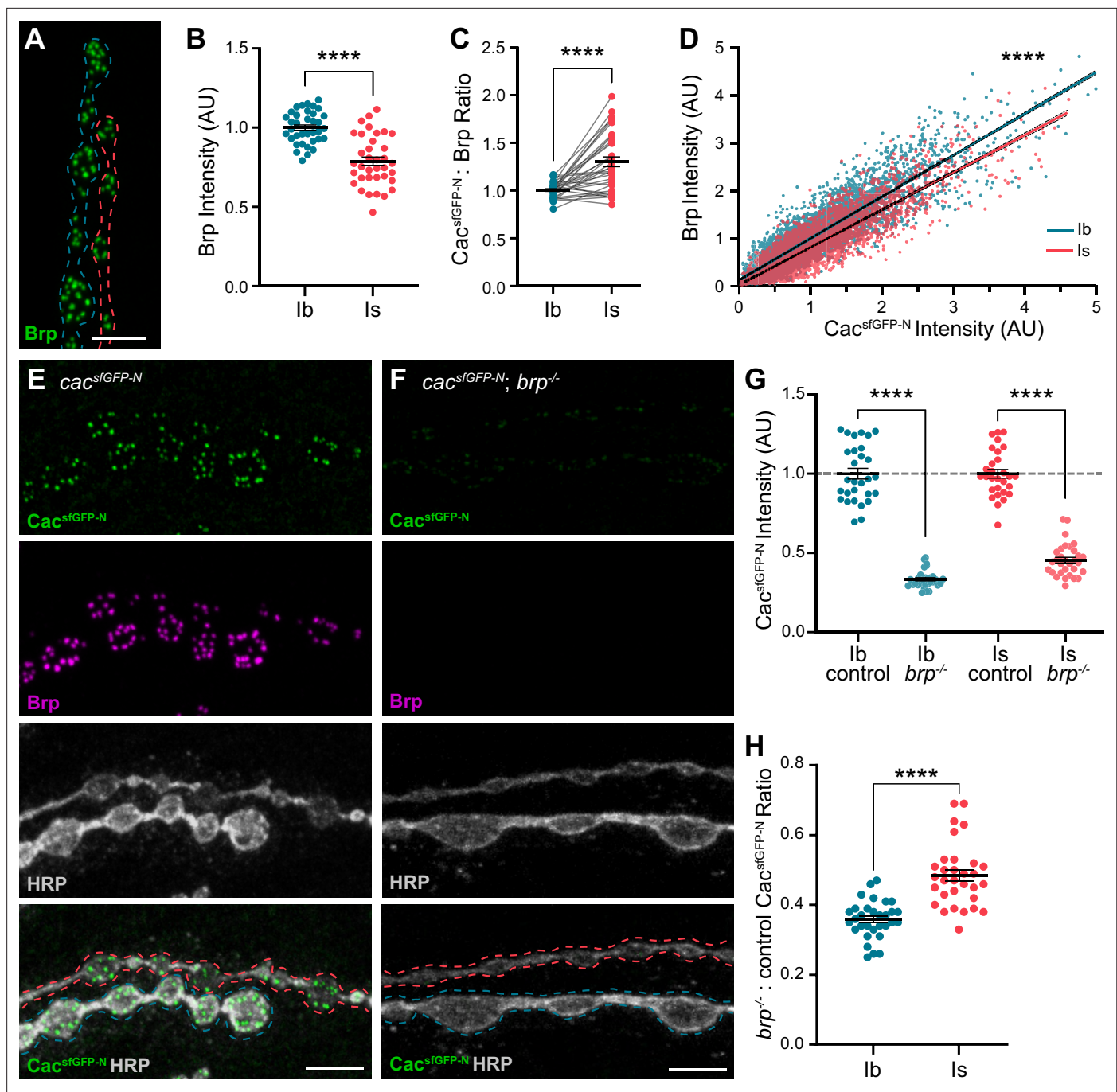


Figure 3. Differences in Bruchpilot (Brp) levels and function at low- and high-P inputs. **(A)** Representative confocal Z-projection of Brp expression at type Ib (blue outline) and type Is (red outline) terminals. **(B)** Quantification of Brp AZ intensity at type Ib and Is terminals. **(C)** Ratio of normalized $Cac^{sfGFP-N}$:Brp levels at type Ib and Is inputs to the same muscles. **(D)** Correlation of $Cac^{sfGFP-N}$ and Brp at type Ib and Is single AZs with linear regression lines (blue and red, respectively) and 95% confidence intervals (black dotted lines) indicated. **(E, F)** Representative confocal Z-projections of $Cac^{sfGFP-N}$ (green), Brp (magenta), HRP (white), and merge at type Ib (blue outline) and Is (red outline) terminals of $cac^{sfGFP-N}$ (control) or $cac^{sfGFP-N};brp^{-/-}$ ($brp^{-/-}$) animals. **(G)** Quantification of $Cac^{sfGFP-N}$ normalized fluorescence intensity at type Ib and Is AZs of control vs $brp^{-/-}$ NMJs. **(H)** Ratio of $Cac^{sfGFP-N}$ fluorescence intensity at type Ib and Is AZs between $brp^{-/-}$ and control NMJs. For B and G, each data point represents the average normalized single AZ sum intensity for an individual NMJ. All scale bars = 5 μ m, all error bars indicate S.E.M., **** $p < 0.0001$. N's, absolute values, and statistical information is detailed in **Supplementary file 1a**.

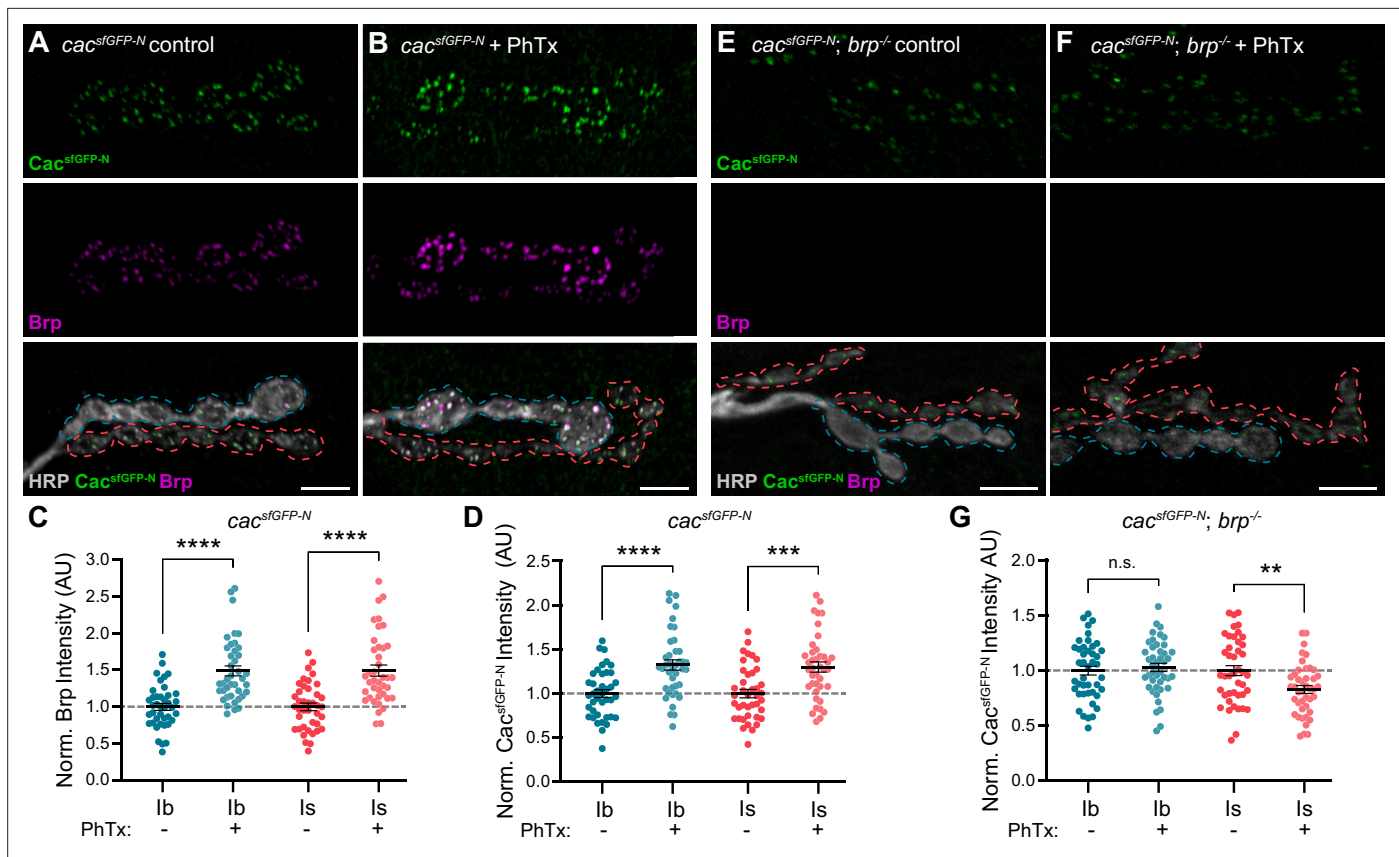


Figure 4. Brp differentially regulates VGCC dynamics at low- and high- P_r inputs during *presynaptic homeostatic potentiation*. **(A, B)** Representative confocal Z-projections of $Cac^{sfGFP-N}$ (top, green), Brp (middle, magenta), and both merged with HRP (bottom, gray) at untreated and PhTx-treated *cac^{sfGFP-N}* NMJs showing type Ib (blue) and type Is (red) terminals. **(C)** Quantification of Brp fluorescence intensity at untreated and PhTx-treated type Ib and Is terminals. **(D)** Quantification of $Cac^{sfGFP-N}$ fluorescence intensity at untreated and PhTx-treated type Ib and Is terminals. **(E, F)** Representative confocal Z-projections of $Cac^{sfGFP-N}$ (top, green), Brp (middle, magenta), and both merged with HRP (bottom, gray) at untreated and PhTx-treated *cac^{sfGFP-N}; brp^{-/-}* NMJs showing type Ib (blue) and type Is (red) terminals. **(G)** Quantification of $Cac^{sfGFP-N}$ fluorescence intensity at untreated and PhTx-treated *cac^{sfGFP-N}; brp^{-/-}* type Ib and Is terminals. For all quantifications, each data point represents the average normalized single AZ sum intensity for an individual NMJ. All scale bars = 5 μ m, all error bars indicate S.E.M. **** $p < 0.0001$; *** $p < 0.001$; ** $p < 0.01$; ns, not significant. N's, absolute values, and statistical information is detailed in **Supplementary file 1a**.

despite their distinct baseline transmission and organizational properties, PhTx-induced potentiation of neurotransmitter release involves the rapid accumulation of VGCCs at both low- and high- P_r AZs.

At low- P_r type Ib AZs, Brp is a critical regulator of PHP-induced accumulation of proteins associated with SV priming and release, specifically Unc13A and Syntaxin-1A (Böhme et al., 2019). At type Ib AZs, PhTx also induces a Brp-dependent increase in Cac density and decrease in channel mobility (Ghelani et al., 2023). Notably, Brp itself becomes more densely organized during PHP (Ghelani et al., 2023), consistent with its denser organization at high- P_r type Is AZs (Mrestani et al., 2021). Since baseline accumulation of VGCCs depends less on Brp at high- P_r type Is AZs, we investigated the role of Brp in promoting dynamic increases in VGCC levels at type Ib and Is AZs by treating *cac^{sfGFP-N}; brp^{-/-}* larvae with PhTx followed by quantification of $Cac^{sfGFP-N}$ levels (Figure 4E and F). We find that PhTx failed to induce accumulation of Cac at either type Ib or Is AZs in *brp^{-/-}* mutants, demonstrating a shared requirement for Brp in regulating VGCC dynamics at both inputs (Figure 4G). In contrast to no change at type Ib AZs, $Cac^{sfGFP-N}$ levels are significantly decreased at type Is AZs (Figure 4G), revealing an input-specific role for Brp in maintaining VGCC levels during the dynamic reorganization of AZs. Consistently, Ghelani et al., 2023 found that whereas PhTx induces a decrease in Cac mobility at wild-type type Ib AZs, in *brp^{-/-}* mutants Cac mobility increases (Ghelani et al., 2023). Together, these findings suggest potentiating synapses must coordinate the accumulation of new VGCCs with

the stabilization of existing channels, and that meeting this challenge is more dependent upon Brp at high-P, AZs.

Endogenous tagging of VGCC auxiliary subunits reveals distinct synaptic expression patterns

In addition to the pore-forming α subunits, VGCCs comprise auxiliary $\alpha 2\delta$ and β subunits that regulate forward channel trafficking, membrane insertion, and function (Figure 5A; Campiglio and Flucher, 2015; Dolphin and Lee, 2020; Weiss and Zamponi, 2017). β subunits interact with pore-forming α subunits intracellularly, whereas GPI-anchored $\alpha 2\delta$ subunits are largely extracellular. Beyond their interaction with α subunits, $\alpha 2\delta$ s have been shown to interact with a growing number of extracellular proteins to promote synaptogenesis (Bauer et al., 2010; Dolphin, 2018; Risher et al., 2018). The *Drosophila* genome encodes one synaptic Ca_v2 α subunit (Cac), one β subunit, and three $\alpha 2\delta$ subunits (Littleton and Ganetzky, 2000). Auxiliary subunits are both spatially and temporally regulated and broadly able to interact with α subunits. Thus, the subunit composition of channel complexes is a potential source of significant diversity in both the spatial and functional regulation of VGCCs.

Ca- β encodes the sole *Drosophila* β subunit and has been shown to enhance Ca^{2+} transients in sensory neurons (Kanamori et al., 2013). *Drosophila* $\alpha 2\delta$ -3, also known as Straightjacket (Stj), has well-characterized roles at the NMJ in promoting Ca^{2+} channel clustering, homeostatic plasticity, and, independently of Cac, synapse formation and organization (Dickman et al., 2008; Hoover et al., 2019; Kurshan et al., 2009; Ly et al., 2008; Schöpf et al., 2021; Wang et al., 2016). While low sequence homology between $\alpha 2\delta$ subunits within and across species makes 1:1 mapping difficult, the remaining two *Drosophila* $\alpha 2\delta$ s map more closely to mammalian $\alpha 2\delta$ -3 and -4 than $\alpha 2\delta$ -1 and -2. Stolid was recently shown to promote dendritic Cac expression in motor neurons, whereas Ma2d is known to function in muscle where it is broadly expressed (Heinrich and Ryglewski, 2020; Reuveny et al., 2018). The synaptic localization of endogenous auxiliary subunits with VGCCs remains unknown in *Drosophila*.

To explore potential differences in VGCC subunit composition at type Ib and Is synapses, we used CRISPR gene editing to incorporate endogenous V5 tags in sequence common to all isoforms of *stj*, *stolid*, and *Ca- β* (Bruckner et al., 2017; Gratz et al., 2014). We inserted V5 after the N-terminal signal peptides of Stj and Stolid and near the C-terminus of *Ca- β* (see Materials and methods for details), and confirmed that the incorporation of the peptide tags did not impair neurotransmission (Figure 5B–E). We investigated the expression of each endogenously tagged subunit in the larval ventral ganglion and found that all subunits are expressed in the synaptic neuropil in a pattern similar to the α subunit Cac (Figure 5F–H; Gratz et al., 2019). Similar to Cac, *Ca- β* ^{V5-C} is highly enriched in the mushroom bodies of the larval brain. We next investigated expression at the larval NMJ where Cac localizes in a single punctum at each AZ and found that only *Ca- β* ^{V5-C} and Stj^{V5-N} are present (Figure 5F–H). This aligns with the recent finding that Stolid does not play a role in regulating Ca^{2+} transients at the larval NMJ (Heinrich and Ryglewski, 2020). We also observe *Ca- β* ^{V5-C} expression in muscle as expected for the sole *Drosophila* β subunit (Figure 5F and see Figure 6C).

Stj/ $\alpha 2\delta$ -3 levels are lower at AZs of high-P, type Is inputs

To investigate *Ca- β* ^{V5-C} and Stj^{V5-N} localization at type Ib and Is AZs, we used super-resolution optical reassignment microscopy. Both subunits localize to AZs labeled with Cac or the CAST/ELKS AZ cytomatrix protein Brp (Figure 6A and B). We observe Brp rings surrounding puncta of VGCCs including *Ca- β* ^{V5-C} (Figure 6A). The tight localization of both subunits to central AZ puncta suggests they are associated with α subunits and predicts that *Ca- β* ^{V5-C} and Stj^{V5-N} levels, like Cac, will be similar at the low- and high-P, synapses. To test this, we imaged *Ca- β* ^{V5-C} and Stj^{V5-N} levels at both inputs simultaneously using confocal microscopy and measured fluorescence intensity (Figure 6C and D). As predicted, we found that *Ca- β* ^{V5-C} levels are similar at type Ib and Is AZs (Figure 6E). In contrast, Stj^{V5-N} levels are significantly lower at high-P, type Is AZs (Figure 6F). Thus, while Cac and *Ca- β* are present in similar ratios at AZs of both inputs, surprisingly, the same is not true of Stj/ $\alpha 2\delta$ -3 with high-P, type Is AZs exhibiting lower levels of Stj. This unexpected finding indicates that α : $\alpha 2\delta$ -3 stoichiometry is not always 1:1 in vivo and differs at low- and high-P, synapses. This is consistent with studies of mammalian subunits indicating that in contrast to β subunits, $\alpha 2\delta$ interactions with α subunits may be transient,

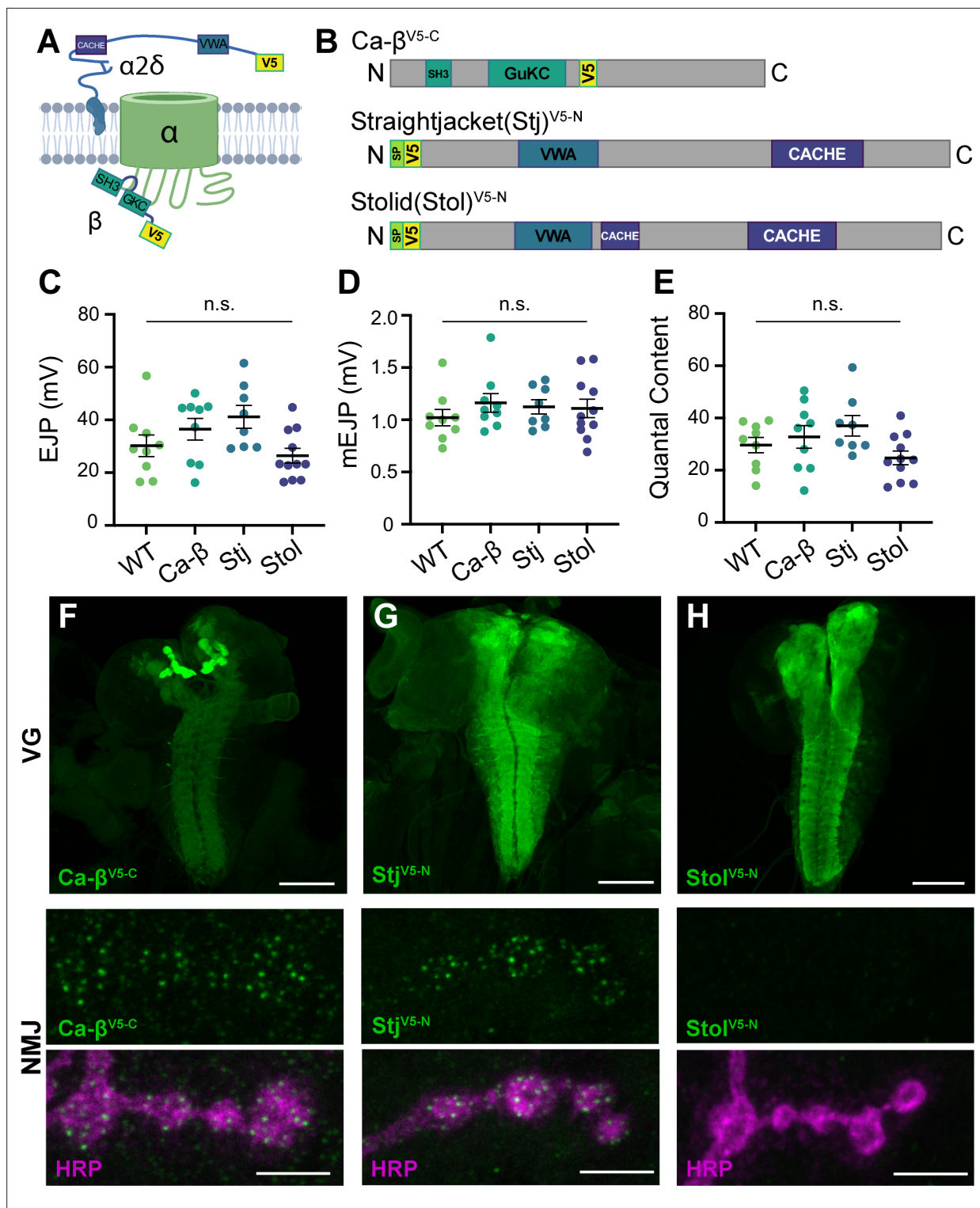


Figure 5. Endogenous tagging of VGCC auxiliary subunits reveals distinct synaptic expression patterns. **(A)** Schematic of a Ca^{2+} channel complex with tagged auxiliary subunits (created with BioRender). **(B)** Schematic of $\text{Ca-}\beta$ (isoform PL shown), Stj (isoform PC), and Stolid (isoform H/I) indicating endogenous tag locations. **(C–E)** Quantification of EJPs, mEJPs, and quantal content for each endogenously tagged line. **(F–H)** Representative confocal Z-projections of auxiliary subunit expression (green) at the larval ventral ganglion (VG, top, scale bars = 100 μm) and NMJs co-labeled with anti-HRP (magenta, bottom, scale bars = 5 μm). All error bars indicate S.E.M., ns, not significant. N's, absolute values, and statistical information is detailed in **Supplementary file 1a**.

© 2024, BioRender Inc. Figure 5A was created using BioRender, and is published under a CC BY-NC-ND license. Further reproductions must adhere to the terms of this license.

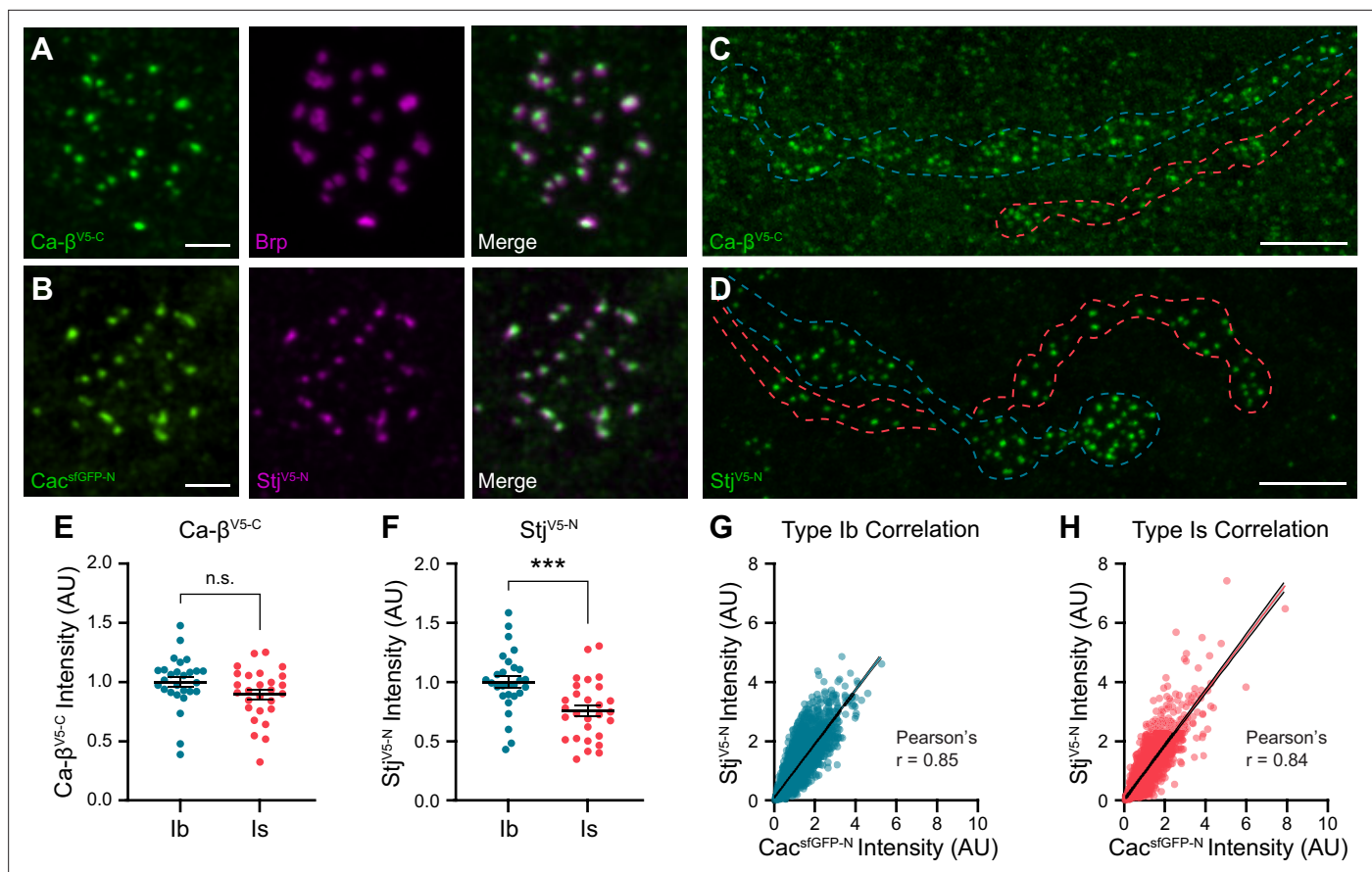


Figure 6. *Stj/α2δ-3* levels are lower at AZs of high- P_r type Is inputs. **(A)** Representative SoRa Z-projections of $\text{Ca-}\beta^{\text{V5-C}}$ (green), Brp (magenta), and merge at a single bouton. **(B)** Representative SoRa Z-projections of $\text{Cac}^{\text{sfGFP-N}}$ (green), $\text{Stj}^{\text{V5-N}}$ (magenta), and merge at a single bouton. Scale bars for A and B=1 μm . **(C, D)** Representative confocal Z-projections of $\text{Ca-}\beta^{\text{V5-C}}$ expression and $\text{Stj}^{\text{V5-N}}$ expression at type Ib (blue outline) and type Is (red outline) terminals. Scale bars = 5 μm . **(E, F)** Quantification of $\text{Ca-}\beta^{\text{V5-C}}$ and $\text{Stj}^{\text{V5-N}}$ fluorescence intensity at type Ib and Is AZs. Each data point represents the average normalized single AZ sum intensity for an individual NMJ. **(G, H)** Correlation of $\text{Cac}^{\text{sfGFP-N}}$ and $\text{Stj}^{\text{V5-N}}$ fluorescence intensity levels at type Ib and Is single AZs with linear regression lines (blue or red line, respectively) and 95% confidence intervals (black lines). All error bars indicate S.E.M. *** $p < 0.001$; ns, not significant. N's, absolute values, and statistical information is detailed in **Supplementary file 1a**.

leading to a pool of VGCCs lacking $\alpha 2\delta$ (Müller *et al.*, 2010; Voigt *et al.*, 2016). Our results indicate this pool may be present in vivo and larger at high- P_r type Is inputs.

To further investigate the contribution of *Stj* to synaptic heterogeneity, we analyzed the relationship between *Cac* and *Stj* levels at individual AZs of type Is inputs. $\text{Stj}^{\text{V5-N}}$ and $\text{Cac}^{\text{sfGFP-N}}$ levels are highly positively correlated at type Is AZs (Figure 6G). We observe the same relationship between $\text{Stj}^{\text{V5-N}}$ and $\text{Cac}^{\text{sfGFP-N}}$ levels at type Ib AZs (Figure 6H). Because P_r is highly positively correlated with *Cac* levels within synaptic subtypes, this indicates that *Stj* levels are also positively correlated with P_r within, but not between, inputs.

***Stj/α2δ-3* levels are modulated at AZs of both low- and high- P_r inputs during presynaptic homeostatic potentiation**

$\alpha 2\delta$ subunits are critical regulators of α subunit forward trafficking. In flies and mammals, overexpression of $\alpha 2\delta$ subunits increases α subunit abundance, whereas overexpression of the α subunit alone does not (Cao *et al.*, 2004; Cunningham *et al.*, 2022; Hoppa *et al.*, 2012). These findings suggest that $\alpha 2\delta$ may be dynamically regulated together with *Cac* during PHP, a prediction we can now test with our endogenously tagged line. Following PhTx exposure, we find that $\text{Stj}^{\text{V5-N}}$ is recruited on a rapid timescale to both low- and high- P_r AZs, increasing by a similar percentage at both type Ib and Is AZs (27% and 26%, respectively) as predicted (Figure 7A-C). *Cac* levels are similarly increased (33% at type Ib and 30% at type Is; See Figure 4D), suggesting coordinated regulation. We have previously

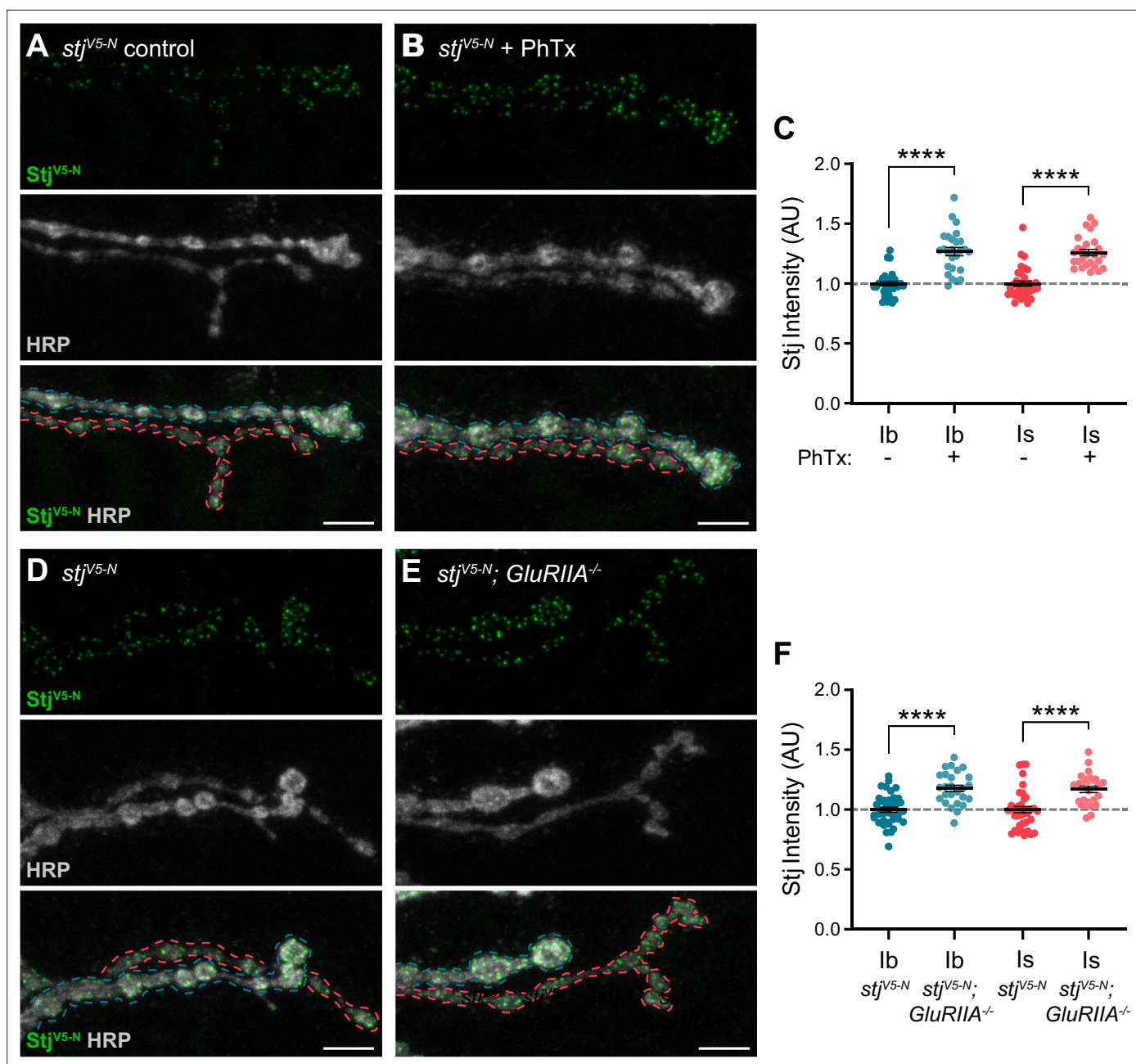


Figure 7. Stj/ $\alpha 2\delta$ -3 levels are modulated at AZs of both low- and high-P, inputs during presynaptic homeostatic potentiation. (A, B) Representative confocal Z-projections of Stj^{V5-N} (top, green), HRP (middle, gray), and merge (bottom) at untreated and PhTx-treated *stj^{V5-N}* NMJs showing type Ib (blue) and type Is (red) terminals. (C) Quantification of Stj^{V5-N} fluorescence intensity at untreated and PhTx-treated type Ib and Is terminals. (D–E) Representative confocal Z-projections of Stj^{V5-N} (top, green), HRP (middle, gray), and merge (bottom) at *stj^{V5-N}* and *stj^{V5-N}; GluRIIA^{-/-}* NMJs showing type Ib (blue) and type Is (red) terminals. (F) Quantification of Stj^{V5-N} fluorescence intensity levels at *stj^{V5-N}* and *stj^{V5-N}; GluRIIA^{-/-}* type Ib and Is terminals. For all quantifications, each data point represents the average normalized single AZ sum intensity for an individual NMJ. All scale bars = 5 μ m, all error bars indicate S.E.M. **** $p < 0.0001$. N's, absolute values, and statistical information is detailed in **Supplementary file 1a**.

shown that Cac abundance is also increased in chronic PHP, which is induced by genetic loss of the GluRIIA receptor subunit (Gratz et al., 2019; Li et al., 2018; Petersen et al., 1997). We investigated Stj dynamics in *GluRIIA^{-/-}* null animals and observed elevated Stj^{V5-N} levels at AZs of both type Ib and Is inputs (18% and 17%, respectively; **Figure 7D–F**), indicating similar dynamics during chronic PHP. These data are consistent with the recent finding that in addition to its previously uncovered role in promoting an increase in the readily releasable pool of SVs (Wang et al., 2016), Stj is required for the

accumulation of Cac at type Ib AZs during both acute and chronic PHP (Zhang *et al.*, 2023). Thus, the abundance of multiple key AZ proteins distinguishes low- and high- P_r synapses within, but not between, inputs at baseline and during homeostatic plasticity.

Discussion

Complex nervous system function depends on communication at synapses with heterogeneous and plastic properties. Paradoxical findings in the field have raised questions about the role of VGCCs in establishing neurotransmitter release properties. Our findings suggest a model in which two broad intersecting mechanisms contribute to synaptic diversity in the nervous system: (1) nanoscale spatial organization and relative molecular content establish distinct average basal release probabilities that differ between inputs and (2) coordinated modulation of VGCC and active zone protein abundance independently tunes P_r among individual synapses of distinct inputs. This model provides a framework for integrating diverse findings in the field and understanding how multiple levels of molecular and organizational diversity can intersect to generate extensive synaptic heterogeneity. Investigations at diverse synapses using approaches ranging from cell-attached patch recordings to freeze-fracture immuno-electron microscopy to correlative functional imaging have revealed a strong positive correlation between VGCC number and P_r (Akbergenova *et al.*, 2018; Gratz *et al.*, 2019; Holderith *et al.*, 2012; Miki *et al.*, 2017; Nakamura *et al.*, 2015; Newman *et al.*, 2022; Sheng *et al.*, 2012). This holds true among mature synapses in the hippocampus or immature synapses of the calyx of Held (Holderith *et al.*, 2012; Sheng *et al.*, 2012) and at the developing *Drosophila* NMJ where the differences in P_r and channel number between AZs of a single input also correlate with synapse maturity (Akbergenova *et al.*, 2018; Gratz *et al.*, 2019; Newman *et al.*, 2022). While this conclusion corresponds neatly with the dependence of neurotransmitter release on Ca^{2+} influx, counterintuitively, a disconnect between VGCC and P_r is observed in some studies. Although the number of functional VGCCs positively correlates with P_r among synapses in the immature calyx of Held, the mature calyx has higher P_r yet recruits fewer Ca^{2+} channels (Fedchyshyn and Wang, 2005; Sheng *et al.*, 2012; Wang and Augustine, 2014). Similarly, in the cerebellum, inhibitory stellate cells form high- P_r synapses with lower VGCC levels than low- P_r synapses formed by excitatory granular cells (Rebola *et al.*, 2019). Adding to these paradoxical examples, we find that VGCC levels positively correlate with P_r among the heterogeneous synapses formed by either low- P_r type Ib or high- P_r type Is motor neurons, but overall VGCC abundance is similar at the two inputs (Figures 1 and 2) despite an ~threefold difference in P_r (Lu *et al.*, 2016; Newman *et al.*, 2017). Accordingly, our correlative functional imaging confirms that the same number of channels can support greater release at these high- P_r AZs (Figure 1). While two-fold greater Ca^{2+} influx at high- P_r type Is AZs can explain much of this difference (He *et al.*, 2023; Lu *et al.*, 2016), mounting evidence suggests that here and in other systems differences in P_r are separable from Ca^{2+} influx. At distinct inputs formed by CA1 pyramidal neurons, Ca^{2+} influx is greater at high- P_r synapses, but doesn't explain differences in synaptic strength as raising Ca^{2+} entry at low- P_r synapses to high- P_r synapse levels was not sufficient to increase synaptic strength to high- P_r input levels (Aldahabi *et al.*, 2022). Similar findings have been reported at tonic and phasic synapses of the Crayfish NMJ (Msghina *et al.*, 1999).

The separability of VGCC abundance, Ca^{2+} influx, and P_r appears to be due to molecular and spatial differences between synaptic subtypes. In CA1 pyramidal neurons, differences in Munc-13-dependent SV priming are proposed to establish synapse-specific release properties, possibly due to the presence of distinct isoforms at low- vs. high- P_r connections. In the cerebellum, fewer VGCC are more tightly coupled to SVs at high- P_r stellate synapses (Rebola *et al.*, 2019). More densely organized VGCCs at the mature vs. developing calyx of Held also exhibit greater coupling with SVs (Chen *et al.*, 2015; Fedchyshyn and Wang, 2005; Fekete *et al.*, 2019; Nakamura *et al.*, 2015; Sheng *et al.*, 2012). We find that Cac clusters are denser at high- P_r AZs formed by *Drosophila* phasic motor neurons (Figure 2). Brp, which organizes both VGCCs and SVs, is also more densely organized at type Is synapses (He *et al.*, 2023; Jetli *et al.*, 2023; Mrestani *et al.*, 2021), consistent with an overall more compact organization of high- P_r AZs. A straightforward prediction is that a more compact AZ organization will decrease the distance between VGCCs and SVs. Indeed, a recent electrophysiological study using new tools for genetically isolating type Ib and Is inputs demonstrated that neurotransmitter release at denser type Is synapses is less impacted by the slow Ca^{2+} chelator EGTA than type Ib synapses, indicating tighter VGCC-SV coupling (He *et al.*, 2023). Together, these findings suggest

that more compact AZs may be a common organizing principle of high- P_r synapses. Consistent with this model, Brp and Unc-13 density increase during PHP when P_r is increased (Dannhäuser et al., 2022; Ghelani et al., 2023; Mrestani et al., 2021).

We also observe molecular differences between *Drosophila* motor inputs that may contribute to distinct P_r . Somewhat counterintuitively, high- P_r type Is AZs have lower levels of both Brp and Stj/ $\alpha 2\delta$ -3 (Figures 3 and 6). Brp/CAST/ELKS AZ cytomatrix proteins are central regulators of synapse organization across species (Dai et al., 2006; Dong et al., 2018; Hallermann et al., 2010; Held et al., 2016; Kittel et al., 2006; Liu et al., 2014; McDonald et al., 2020; Radulovic et al., 2020). Brp interacts broadly with AZ proteins to promote Cac clustering, organize SVs, and recruit Unc13A, which defines SV release sites (Böhme et al., 2016; Fulterer et al., 2018; Ghelani et al., 2023; Liu et al., 2011). While Brp clearly plays a central role in AZ organization and reorganization, we also find that type Ib and Is synapses have distinct requirements for Brp during synapse formation and homeostatic potentiation (Figures 3 and 4). Synapse-specific roles for Brp are supported by a recent functional imaging study in *Drosophila* (Jetti et al., 2023) and studies of ELKS at mammalian inhibitory and excitatory synapses (Held et al., 2016), and suggest additional factors establish neuron-specific differences in Brp dependence. A recent single-cell transcriptomic study of type Ib and Is motor neurons provides an unbiased starting point for identifying candidate regulators of molecular differences at low- and high- P_r AZs (Jetti et al., 2023). Differentially expressed genes encode cytoskeletal and motor-related proteins, regulators of proteostasis, and post-translational modifying enzymes/pathway components – all of which could potentially contribute to establishing the observed molecular and/or spatial differences between type Ib and Is AZs. The VGCC complex itself provides an additional potential mechanism for diversifying synaptic function. Both β and $\alpha 2\delta$ subunits can influence the membrane localization and function of VGCCs (Campiglio and Flucher, 2015; Dolphin and Lee, 2020; Weiss and Zamponi, 2017). In addition to the ability to mix and match subunits, many of the genes encoding VGCC subunits across species are extensively alternatively spliced to generate additional functional diversity (Cingolani et al., 2023; Lipscombe et al., 2013; Lipscombe and Lopez Soto, 2019) – an area of great interest for further investigation at the *Drosophila* NMJ. Because both β and $\alpha 2\delta$ subunits are generally considered positive regulators of channel trafficking and function, we were surprised to find upon endogenously tagging Stj/ $\alpha 2\delta$ -3 that its levels are lower at high- P_r AZs (Figures 5 and 6). Since AZ levels of α subunit Cac are similar at the two inputs, lower levels of Stj at type Is synapses indicates a difference in α : $\alpha 2\delta$ -3 stoichiometry between low- and high- P_r synaptic subtypes. While some previous studies have observed a tight association between the two subunits, a single-molecule tracking and modeling study of mammalian VGCCs found that $\alpha 2\delta$ subunits have a relatively low affinity for α subunits and predicted a population of α subunits not associated with an $\alpha 2\delta$ subunit (Cassidy et al., 2014; Voigt et al., 2016). Consistently, whereas α and β subunits were isolated at near equimolar ratios following affinity purification of Ca_v2 channels, molar levels of $\alpha 2\delta$ were a surprising 90% lower (Müller et al., 2010). Our findings suggest there may be a pool of VGCCs lacking an $\alpha 2\delta$ subunit at endogenous synapses, and further suggest that this pool is specific to or enriched at high- P_r type Is AZs. Stj is both required (Dickman et al., 2008; Kurshan et al., 2009; Ly et al., 2008) and rate limiting (Cunningham et al., 2022) for Cac accumulation at AZs. Stj does not appear to function in the stabilization of channels at the AZ membrane, but rather at an upstream step in the progression from ER to plasma membrane (Cunningham et al., 2022), so complexes may not need to be maintained. However, a recent study in *C. elegans* suggested that auxiliary subunits to promote stabilization in the membrane, raising the possibility that the difference observed in $\alpha 2\delta$ levels could translate to a difference in α subunit mobility within Ib vs. Is AZs (Oh et al., 2023). Tools for following Stj dynamics in developing neurons will help clarify its precise role in Cac delivery at type Ib and Is AZs.

How might a higher α : $\alpha 2\delta$ -3 ratio result in higher P_r ? One possibility involves $\alpha 2\delta$ -3 interactions with cell adhesion molecules. In mammals, α -Neurexin specifically inhibits Ca^{2+} currents in $Ca_v2.2$ channels containing $\alpha 2\delta$ -3 (Tong et al., 2017), which, if similar at the *Drosophila* NMJ, could result in greater inhibition of channel function at type Ib AZs and contribute to the observed difference in Ca^{2+} influx. Loss of *Drosophila* Neurexin reduces neurotransmitter release at the NMJ, but it also leads to reduced synaptogenesis so whether this is a direct effect remains unknown (He et al., 2007). Another possibility is that Stj isoforms with different functions are differentially expressed at type Ib and Is AZs. A recent transcriptomic study observed no significant differences in mRNA splice isoforms,

but transcript levels do not always reflect protein levels (Jetti et al., 2023). Notably, we find that among synapses of either low- or high- P_r AZs, Stj levels correlate with P_r and Stj levels are increased across AZs of both inputs during acute and chronic PHP (Figure 7). Cac and Stj levels increase by similar amounts at the two inputs, suggesting the difference in stoichiometry is maintained following homeostatic potentiation. $\alpha 2\delta-3$ is an important drug target for treating epilepsy, neuropathic pain, and anxiety, so understanding its cell-specific roles and how $\alpha:\alpha 2\delta-3$ stoichiometry impacts channel function and contributes to synaptic diversity is of great interest.

Materials and methods

Drosophila genetics and gene editing

The following fly lines used in this study were obtained from the Bloomington *Drosophila* Stock Center (BDSC, NIH P40OD018537): w^{1118} (RRID:BDSC_5905), *vasa-Cas9* (RRID:BDSC_51324), piggyBac transposase (RRID:BDSC_8283), and *Df(2 R)brp^{6.1}* (Gratz et al., 2014; Horn et al., 2003). *brp⁶⁹* and *GluRIIA^{sp16}* (*GluRIIA^{-/-}*) alleles were generously provided by Stephan Sigrist (Freie Universität Berlin; Fouquet et al., 2009; Kittel et al., 2006) and Aaron DiAntonio (Peterson et al., 1997) respectively. *brp* loss-of-function experiments were performed in *brp⁶⁹/Df(2 R)brp^{6.1}*. *Drosophila melanogaster* stocks were raised on molasses food (Lab Express, Type R) in a 25 °C incubator with controlled humidity and 12 hr light/dark cycle. Endogenously tagged *cac*, *Ca-β*, *stolid*, and *straightjacket* (*stj*) alleles were generated using our piggyBac-based CRISPR approach as previously detailed (https://flycrispr.org; Bruckner et al., 2017; Gratz et al., 2019). We used FlyBase (release FB2024_01) to obtain genomic sequences (doi.org/10.1093/genetics/iyad211). Td-Tomato and Halo tags were incorporated at the N-terminus of Cac, where we have previously incorporated fluorescent tags (Ghelani et al., 2023; Gratz et al., 2019). V5 tags were incorporated at the N-terminus of Stj and Stolid after their signal peptide sequences, immediately after Asparagine 34 of Stj and after Isoleucine 34 of Stolid. For Ca-β, V5 was inserted immediately after Proline 446 of isoform Ca-β-PN. All endogenously tagged lines are fully viable in homozygous males and females and were molecularly confirmed by Sanger sequencing. All genetic reagents generated in this study are available upon request. gRNAs sequences used:

cac^{HaloTag-N} / cac^{Td-Tomato-N}: CATCGCTTAGCTGATAGAATGG
stj^{V5-N}: GCTGGCTGCAGATTGACGCACGG
stolid^{V5-N}: ATTTGTTGCATTCCCGATCAGG
Ca-β^{V5-C}: CTCCGCAGATCCCGCGCTCTGG

Immunostaining

All antibodies used, associated fixation methods, and incubation times can be found in **Supplementary file 1b**. Male wandering third-instar larvae were dissected in ice-cold saline and fixed either for 6 min at room temperature with Bouin's fixative, 5 min on ice with 100% methanol, or 30 min at room temperature (RT) in 4% PFA. Dissections were permeabilized with PTX (PBS with 0.1% Triton-X 100) and blocked for 1 hr at RT using 5% goat serum and 1% bovine serum albumin. Stained larvae were mounted in Vectashield (Vector Laboratories, #H-1000) under Fisherbrand coverglass (Fisher Scientific, #12541B) for confocal microscopy, with Prolong glass mounting medium (Thermo Fisher Scientific, #P36980) under Zeiss High Performance Coverglass (Zeiss, #474030-9000-000) for super-resolution optical reassignment microscopy, or buffer (see STORM imaging and analysis section) under Zeiss coverglass with edges sealed using vacuum grease for STORM microscopy.

Ca²⁺ imaging and analysis

Functional imaging was performed on a Nikon A1R resonant scanning confocal mounted on a FN1 microscope using a Nikon Apo LWD 25x1.1 NA objective and a Mad City Labs piezo drive nosepiece. Dissections and data collection were performed as previously described in Gratz et al., 2019. Briefly, *cac^{Td-Tomato-N}*, *Mhc-GCaMP6f* male 3rd instar larvae were dissected in HL3 containing 0.2 mM Ca²⁺ and 25 mM Mg²⁺ with motor axons severed and the larval brain removed. Larval filets were placed in HL3 containing 1.5 mM Ca²⁺ and 25 mM Mg²⁺ for recording. Nerves were suctioned into 1.5 mm pipettes and stimulus amplitude was adjusted to recruit both type Ib and Is inputs. Motor terminals from segments A2-4 at NMJ 6/7 were imaged for Cac^{Td-Tomato-N} levels first using a galvanometer scanner,

then a resonant scanner to collect GCaMP6f events in a single focal plane continuously for 120 stimulations at a 0.2 Hz stimulation frequency.

Z-stacks and movies were loaded into Nikon Elements Software (NIS) where movies were motion corrected, background subtracted, and denoised. Change in fluorescence (ΔF) movies were then created by subtracting the average of the previous 10 frames from each frame. A substack of only stimulation frames was further processed using a gaussian filter followed by the Bright Spots detection module in the Nikon GA3 software to identify the location of each postsynaptic event. $\text{Cac}^{\text{Td-Tomato-N}}$ fluorescence intensity levels and coordinate locations were measured for 531 AZs for type Ib and 365 AZs for type Is terminals across six animals. X-Y coordinate positions of fluorescent signals from GCaMP6f postsynaptic events were aligned to $\text{Cac}^{\text{Td-Tomato-N}}$ puncta locations and each post synaptic event assigned to a Cac punctum using nearest neighbor analysis. Postsynaptic events that did not map within 960 nm of a $\text{Cac}^{\text{Td-Tomato-N}}$ punctum were discarded from the analysis. Pearson's correlation was used to determine the correlation between P_r and Cac levels normalized to average to account for variability between imaging sessions. Cac intensity- P_r heat maps were generated using Python matplotlib and seaborn plotting packages.

STORM imaging and analysis

STORM imaging was performed on a Nikon Eclipse Ti2 3D NSTORM with an Andor iXon Ultra camera, Nikon LUN-F 405/488/640 nm lasers, and a Nikon 100x1.49 NA objective. STORM buffer (10 mM MEA (pH 8.0), 3 U/mL pyranose oxidase, and 90 U/mL catalase, 10% (w/v) glucose, 10 mM sodium chloride, and 50 mM Tris hydrochloride) was made fresh each imaging day and pH adjusted to between 7.0–8.0 using acetic acid. $\text{cac}^{\text{HaloTag-N}}$ NMJs were labeled as detailed in **Supplementary file 1b** and immediately imaged for HRP in 488 channel to identify type Ib and Is terminals. $\text{Cac}^{\text{HaloTag-N}}$ was then imaged using the 640 nm laser line at 33 Hz for 5000 frames. 405 nm laser power was gradually increased over the course of imaging to compensate for run-down of blinking rates. A back aperture camera was used to ensure beam focus and position for each imaging session to ensure high signal to noise. Data were binned with a CCD minimum threshold of 100 and drift correction was applied using the NIS Software STORM package. ROIs of single boutons were drawn in NIS using HRP in the 488 nm channel followed by a DBSCAN analysis with criteria of 10 molecules within 50 nm to determine clusters. Positional coordinates of localizations within clusters from DBSCAN were exported from NIS and run through a Python script published with this manuscript. Using the implementation developed in *Mrestani et al., 2021* as a starting point, we wrote custom code to use the alpha shapes component of the CGAL package (<https://www.cgal.org>), via a python wrapper (<https://anaconda.org/conda-forge/cgal>), to measure the area of Ca^{2+} channel clusters, the number of localizations, and calculate cluster density. To achieve an average lateral localization accuracy of ~30 nm, all localizations with >50 nm localization accuracy were removed prior to analysis. Using this custom code, $\text{Cac}^{\text{HaloTag-N}}$ area was analyzed using an alpha value of 0.015, which controls the complexity of cluster boundaries (not restricted to be convex).

Confocal imaging and analysis

For quantitative AZ analysis of larval NMJs, dissections stained in the same dish were imaged on a Nikon Eclipse Ni A1R+confocal microscope using an Apo TIRF 60x1.49 NA oil-immersion objective for larval NMJs. NMJs containing both type Is and type Ib branches from muscles 6/7 in segments A2-4 were collected. ROIs were drawn using HRP staining to differentiate between type Ib and Is branches. To analyze individual AZs, Nikon Elements GA3 Software was used to process images with Gaussian and rolling ball filters and measure fluorescence intensity levels at individual puncta identified by the Bright Spots module. When experimental design allowed, Brp fluorescence signal was used to create a binary mask to aid in the identification of AZ ROIs for analysis. Otherwise, binary masks were created based on the fluorescence signal of the channel analyzed. Quantifications were conducted masked to genotype and/or treatment. Confocal fluorescence intensity level data are reported as the sum fluorescence intensity per AZ averaged over individual NMJs. For **Figure 5**, larvae were stained separately and imaged using a Nikon Plan-Apo 20x0.75 NA objective (ventral ganglia) or Apo TIRF 60x1.49 NA oil-immersion objective (NMJs). Super-resolution optical reassignment images were obtained on a Nikon CSU-W1 SoRa (Spinning Disk Super Resolution by Optical Pixel Reassignment)

with a Photometrics Prime BSI sCMOS camera and a 60x1.49 NA oil-immersion objective. Images were acquired using Nikon NIS and deconvolved using Richardson-Lucy deconvolution with 15–20 iterations.

Electrophysiology

Current-clamp recordings were performed as previously described (*Bruckner et al., 2017*). Male third-instar larvae were dissected in HL3 (70 mM NaCl, 5 mM KCl, 15 mM MgCl₂, 10 mM NaHCO₃, 115 mM sucrose, 5 mM trehalose, 5 mM HEPES, pH 7.2) with 0.25 mM Ca²⁺. Recordings were performed in HL3 at the external Ca²⁺ concentration indicated. Sharp borosilicate electrodes filled with 3 M KCl were used to record from muscle 6 of abdominal segments A3 and A4. Recordings were conducted on a Nikon FN1 microscope using a 40x0.80 NA water-dipping objective and acquired using an Axoclamp 900 A amplifier, Digidata 1550B acquisition system, and pClamp 11.0.3 software (Molecular Devices). For each cell with an initial resting potential between –60 and –80 mV and input resistance ≥5 MΩ, mean miniature excitatory junctional potentials (mEJPs) were collected for 1 min in the absence of stimulation and analyzed using Mini Analysis (Synaptosoft). EJPs were generated by applying a stimulus to severed segmental nerves at a frequency of 0.2 Hz using an isolated pulse stimulator 2100 (A-M Systems). Stimulus amplitude was adjusted to consistently elicit compound responses from both type Ib and Is motor neurons. At least 25 consecutive EJPs were recorded for each cell and analyzed in pClamp to obtain mean amplitude. Quantal content was calculated for each recording as mean EJP amplitude divided by mean mEJP amplitude.

Acute homeostatic challenge

Acute PHP was induced by incubating semi-intact preparations in 20 μM Philanthotoxin-433 (**Figure 4**: PhTx; Santa Cruz, sc-255421, Lot B1417 and **Figure 7**: PhTx; Sigma Aldrich, P207-2, Lot MKCK7405) diluted in HL3 containing 0.4 mM Ca²⁺ for 10 min at room temperature (*Frank et al., 2006*). Control preparations were given a mock treatment. Following control and experimental treatment, dissections were completed, fixed in 4% PFA for 30 min (*cac^{stGFP-N}*) or 100% ice-cold methanol on ice for 5 min (*stj^{v5-N}*), and stained in the same dish. Analyses of fluorescent intensity levels were performed as previously described in the *Confocal imaging and analysis* section.

Experimental design and statistical analysis

Statistical analyses were conducted in GraphPad Prism 9. Normality was determined by the D'Agostino–Pearson omnibus test. Comparisons of normally distributed data were conducted by Student's *t* test (with Welch's correction in the case of unequal variance) for single comparisons and ANOVA followed by Tukey's test for multiple comparisons. For non-normally distributed data, the Mann–Whitney *U* test and Kruskal–Wallis test followed by Dunn's multiple comparisons tests were used for single and multiple comparisons, respectively. Paired analysis of non-normally distributed data was conducted using Wilcoxon's matched-pairs signed rank test. One-dimensional Pearson correlation coefficients (*r*) were used to compare intensity levels and neurotransmitter release probability. ANCOVA test was performed on all regression lines to determine if slopes were significantly different. Reported values are mean ± SEM. Sample size, statistical test, and *p* values for each comparison are reported in **Supplementary file 1a**. All source data, including statistical tests and raw images, can be found in the following Harvard Dataverse dataset <https://doi.org/10.7910/DVN/GGP3UM>.

Acknowledgements

We thank the Developmental Studies Hybridoma Bank, the Bloomington Drosophila Stock Center (NIH P40OD018537), Flybase (*Öztürk-Çolak et al., 2024*), Ehud Isacoff (UC Berkeley), and Stephan Sigrist (Freie Universität Berlin) for providing antibodies and fly stocks. The Nikon SoRa/STORM microscope was generously provided by The Neurobiology of Cells and Circuits/Center for Translational Neuroscience Microscopy Committee, Carney Institute for Brain Science. We are grateful to Joel Hirsch (Tel Aviv University) for consultations on tagging Ca-β, Nicholas Deakin (Nikon) for guidance on STORM imaging, the Heckmann lab (University of Würzburg) for guidance on STORM image analysis pipelines, Matthew Knoepfel for help generating CRISPR alleles, and Liana Lewis for her assistance with image analysis. We thank Rajan Thakur and the members of the O'Connor-Giles lab for thoughtful discussions and comments on the manuscript. This work was supported by grants from the National

Institute of Neurological Disorders and Stroke, National Institutes of Health to KMOG (R01NS078179) and ATM (F31NS122424), Brown Neuroscience Graduate Program training grant T32 MH020068, and funds from the Brown University Carney Institute for Brain Science.

Additional information

Funding

Funder	Grant reference number	Author
National Institute of Neurological Disorders and Stroke	R01NS078179	Kate M O'Connor-Giles
National Institute of Neurological Disorders and Stroke	F31NS122424	Audrey T Medeiros
Brown Neuroscience Graduate Program	T32 MH020068	Audrey T Medeiros

The funders had no role in study design, data collection, and interpretation, or the decision to submit the work for publication.

Author contributions

Audrey T Medeiros, Conceptualization, Resources, Data curation, Software, Formal analysis, Funding acquisition, Validation, Investigation, Visualization, Methodology, Writing – original draft, Project administration, Writing – review and editing; Scott J Gratz, Conceptualization, Resources, Data curation, Software, Formal analysis, Supervision, Funding acquisition, Validation, Investigation, Visualization, Methodology, Writing – original draft, Project administration, Writing – review and editing; Ambar Delgado, Data curation, Formal analysis, Investigation, Writing – review and editing; Jason T Ritt, Software, Formal analysis, Methodology, Writing – review and editing; Kate M O'Connor-Giles, Conceptualization, Data curation, Formal analysis, Supervision, Funding acquisition, Writing – original draft, Project administration, Writing – review and editing

Author ORCIDs

Audrey T Medeiros  <http://orcid.org/0000-0002-5562-4772>

Scott J Gratz  <http://orcid.org/0000-0002-0106-8336>

Jason T Ritt  <https://orcid.org/0000-0003-3113-7977>

Kate M O'Connor-Giles  <https://orcid.org/0000-0002-2259-8408>

Peer review material

Reviewer #1 (Public Review): <https://doi.org/10.7554/eLife.88412.3.sa1>

Reviewer #2 (Public Review): <https://doi.org/10.7554/eLife.88412.3.sa2>

Author response <https://doi.org/10.7554/eLife.88412.3.sa3>

Additional files

Supplementary files

- Transparent reporting form
- Supplementary file 1. Tables detailing absolute values, statistics, and imaging conditions of endogenously-tagged genetic lines.

Data availability

All source data, including statistical tests and raw images, can be found in the following Harvard Dataverse dataset <https://doi.org/10.7910/DVN/GGP3UM>.

The following dataset was generated:

Author(s)	Year	Dataset title	Dataset URL	Database and Identifier
Audrey M	2024	Source data for Medeiros et al., eLife Version of Record	https://doi.org/10.7910/DVN/GGP3UM	Harvard Dataverse, 10.7910/DVN/GGP3UM

References

- Akbergenova Y**, Cunningham KL, Zhang YV, Weiss S, Littleton JT. 2018. Characterization of developmental and molecular factors underlying release heterogeneity at *Drosophila* synapses. *eLife* **7**:e38268. DOI: <https://doi.org/10.7554/eLife.38268>, PMID: 29989549
- Aldahabi M**, Balint F, Holderith N, Lorincz A, Reva M, Nusser Z. 2022. Different priming states of synaptic vesicles underlie distinct release probabilities at hippocampal excitatory synapses. *Neuron* **110**:4144–4161.. DOI: <https://doi.org/10.1016/j.neuron.2022.09.035>, PMID: 36261033
- Aponte-Santiago NA**, Littleton JT. 2020. Synaptic properties and plasticity mechanisms of invertebrate tonic and phasic neurons. *Frontiers in Physiology* **11**:611982. DOI: <https://doi.org/10.3389/fphys.2020.611982>, PMID: 33391026
- Aponte-Santiago NA**, Ormerod KG, Akbergenova Y, Littleton JT. 2020. Synaptic plasticity induced by differential manipulation of tonic and phasic motoneurons in *Drosophila*. *The Journal of Neuroscience* **40**:6270–6288. DOI: <https://doi.org/10.1523/JNEUROSCI.0925-20.2020>, PMID: 32631939
- Ariel P**, Hoppa MB, Ryan TA. 2012. Intrinsic variability in Pv, RRP size, Ca(2+) channel repertoire, and presynaptic potentiation in individual synaptic boutons. *Frontiers in Synaptic Neuroscience* **4**:9. DOI: <https://doi.org/10.3389/fnsyn.2012.00009>, PMID: 23335896
- Atwood HL**, Govind CK, Wu CF. 1993. Differential ultrastructure of synaptic terminals on ventral longitudinal abdominal muscles in *Drosophila* larvae. *Journal of Neurobiology* **24**:1008–1024. DOI: <https://doi.org/10.1002/neu.480240803>, PMID: 8409966
- Atwood HL**, Karunanithi S. 2002. Diversification of synaptic strength: presynaptic elements. *Nature Reviews. Neuroscience* **3**:497–516. DOI: <https://doi.org/10.1038/nrn876>, PMID: 12094207
- Bauer CS**, Tran-Van-Minh A, Kadurin I, Dolphin AC. 2010. A new look at calcium channel alpha2delta subunits. *Current Opinion in Neurobiology* **20**:563–571. DOI: <https://doi.org/10.1016/j.conb.2010.05.007>
- Böhme MA**, Beis C, Reddy-Alla S, Reynolds E, Mampell MM, Grasskamp AT, Lützkendorf J, Bergeron DD, Driller JH, Babikir H, Göttfert F, Robinson IM, O’Kane CJ, Hell SW, Wahl MC, Stelz U, Loll B, Walter AM, Sigrist SJ. 2016. Active zone scaffolds differentially accumulate Unc13 isoforms to tune Ca(2+) channel-vesicle coupling. *Nature Neuroscience* **19**:1311–1320. DOI: <https://doi.org/10.1038/nn.4364>, PMID: 27526206
- Böhme MA**, McCarthy AW, Grasskamp AT, Beuschel CB, Goel P, Jusyte M, Laber D, Huang S, Rey U, Petzoldt AG, Lehmann M, Göttfert F, Haghghi P, Hell SW, Oswald D, Dickman D, Sigrist SJ, Walter AM. 2019. Rapid active zone remodeling consolidates presynaptic potentiation. *Nature Communications* **10**:1085. DOI: <https://doi.org/10.1038/s41467-019-08977-6>, PMID: 30842428
- Branco T**, Staras K. 2009. The probability of neurotransmitter release: variability and feedback control at single synapses. *Nature Reviews. Neuroscience* **10**:373–383. DOI: <https://doi.org/10.1038/nrn2634>, PMID: 19377502
- Bruckner JJ**, Zhan H, Gratz SJ, Rao M, Ukken F, Zilberg G, O’Connor-Giles KM. 2017. Fife organizes synaptic vesicles and calcium channels for high-probability neurotransmitter release. *The Journal of Cell Biology* **216**:231–246. DOI: <https://doi.org/10.1083/jcb.201601098>, PMID: 27998991
- Campiglio M**, Flucher BE. 2015. The role of auxiliary subunits for the functional diversity of voltage-gated calcium channels. *Journal of Cellular Physiology* **230**:2019–2031. DOI: <https://doi.org/10.1002/jcp.24998>, PMID: 25820299
- Cao Y-Q**, Piedras-Rentería ES, Smith GB, Chen G, Harata NC, Tsien RW. 2004. Presynaptic Ca2+ channels compete for channel type-preferring slots in altered neurotransmission arising from Ca2+ channelopathy. *Neuron* **43**:387–400. DOI: <https://doi.org/10.1016/j.neuron.2004.07.014>, PMID: 15294146
- Cassidy JS**, Ferron L, Kadurin I, Pratt WS, Dolphin AC. 2014. Functional exofacially tagged N-type calcium channels elucidate the interaction with auxiliary $\alpha 2\delta$ -1 subunits. *PNAS* **111**:8979–8984. DOI: <https://doi.org/10.1073/pnas.1403731111>, PMID: 24889613
- Chen Z**, Das B, Nakamura Y, DiGregorio DA, Young SM. 2015. Ca2+ channel to synaptic vesicle distance accounts for the readily releasable pool kinetics at a functionally mature auditory synapse. *The Journal of Neuroscience* **35**:2083–2100. DOI: <https://doi.org/10.1523/JNEUROSCI.2753-14.2015>, PMID: 25653365
- Cingolani LA**, Thalhammer A, Jaudon F, Muià J, Baj G. 2023. Nanoscale organization of Ca_v2.1 splice isoforms at presynaptic terminals: implications for synaptic vesicle release and synaptic facilitation. *Biological Chemistry* **404**:931–937. DOI: <https://doi.org/10.1515/hsz-2023-0235>, PMID: 37658578
- Cunningham KL**, Sauvola CW, Tavana S, Littleton JT. 2022. Regulation of presynaptic Ca²⁺ channel abundance at active zones through a balance of delivery and turnover. *eLife* **11**:78648. DOI: <https://doi.org/10.7554/eLife.78648>, PMID: 35833625
- Dai Y**, Taru H, Deken SL, Grill B, Ackley B, Nonet ML, Jin Y. 2006. SYD-2 Liprin-alpha organizes presynaptic active zone formation through ELKS. *Nature Neuroscience* **9**:1479–1487. DOI: <https://doi.org/10.1038/nn1808>, PMID: 17115037

- Dannhäuser S**, Mrestani A, Gundelach F, Pauli M, Komma F, Kollmannsberger P, Sauer M, Heckmann M, Paul MM. 2022. Endogenous tagging of Unc-13 reveals nanoscale reorganization at active zones during presynaptic homeostatic potentiation. *Frontiers in Cellular Neuroscience* **16**:1074304. DOI: <https://doi.org/10.3389/fncel.2022.1074304>, PMID: 36589286
- Davis GW**, Müller M. 2015. Homeostatic control of presynaptic neurotransmitter release. *Annual Review of Physiology* **77**:251–270. DOI: <https://doi.org/10.1146/annurev-physiol-021014-071740>, PMID: 25386989
- Dickman DK**, Kurshan PT, Schwarz TL. 2008. Mutations in a *Drosophila* alpha2delta voltage-gated calcium channel subunit reveal a crucial synaptic function. *The Journal of Neuroscience* **28**:31–38. DOI: <https://doi.org/10.1523/JNEUROSCI.4498-07.2008>, PMID: 18171920
- Dolphin AC**. 2018. Voltage-gated calcium channel $\alpha 2\delta$ subunits: an assessment of proposed novel roles. *F1000Research* **7**:1830. DOI: <https://doi.org/10.12688/f1000research.16104.1>
- Dolphin AC**, Lee A. 2020. Presynaptic calcium channels: specialized control of synaptic neurotransmitter release. *Nature Reviews. Neuroscience* **21**:213–229. DOI: <https://doi.org/10.1038/s41583-020-0278-2>, PMID: 32161339
- Dong W**, Radulovic T, Goral RO, Thomas C, Suarez Montesinos M, Guerrero-Given D, Hagiwara A, Putzke T, Hida Y, Abe M, Sakimura K, Kamasawa N, Ohtsuka T, Young SM. 2018. CAST/ELKS proteins control voltage-gated Ca^{2+} channel density and synaptic release probability at a mammalian central synapse. *Cell Reports* **24**:284–293. DOI: <https://doi.org/10.1016/j.celrep.2018.06.024>, PMID: 29996090
- Eggermann E**, Bucurenciu I, Goswami SP, Jonas P. 2011. Nanodomain coupling between Ca^{2+} channels and sensors of exocytosis at fast mammalian synapses. *Nature Reviews. Neuroscience* **13**:7–21. DOI: <https://doi.org/10.1038/nrn3125>, PMID: 22183436
- Ehmann N**, van de Linde S, Alon A, Ljaschenko D, Keung XZ, Holm T, Rings A, DiAntonio A, Hallermann S, Ashery U, Heckmann M, Sauer M, Kittel RJ. 2014. Quantitative super-resolution imaging of Bruchpilot distinguishes active zone states. *Nature Communications* **5**:4650. DOI: <https://doi.org/10.1038/ncomms5650>, PMID: 25130366
- Fedchyshyn MJ**, Wang LY. 2005. Developmental transformation of the release modality at the calyx of Held synapse. *The Journal of Neuroscience* **25**:4131–4140. DOI: <https://doi.org/10.1523/JNEUROSCI.0350-05.2005>, PMID: 15843616
- Fekete A**, Nakamura Y, Yang YM, Herlitze S, Mark MD, DiGregorio DA, Wang LY. 2019. Underpinning heterogeneity in synaptic transmission by presynaptic ensembles of distinct morphological modules. *Nature Communications* **10**:826. DOI: <https://doi.org/10.1038/s41467-019-08452-2>, PMID: 30778063
- Fouquet W**, Oswald D, Wichmann C, Mertel S, Depner H, Dyba M, Hallermann S, Kittel RJ, Eimer S, Sigrist SJ. 2009. Maturation of active zone assembly by *Drosophila* Bruchpilot. *The Journal of Cell Biology* **186**:129–145. DOI: <https://doi.org/10.1083/jcb.200812150>, PMID: 19596851
- Frank CA**, Kennedy MJ, Goold CP, Marek KW, Davis GW. 2006. Mechanisms underlying the rapid induction and sustained expression of synaptic homeostasis. *Neuron* **52**:663–677. DOI: <https://doi.org/10.1016/j.neuron.2006.09.029>
- Frank CA**. 2014. Homeostatic plasticity at the *Drosophila* neuromuscular junction *Neuropharmacology* **78**:63–74. DOI: <https://doi.org/10.1016/j.neuropharm.2013.06.015>
- Früh SM**, Matti U, Spycher PR, Rubini M, Lickert S, Schlichthaerle T, Jungmann R, Vogel V, Ries J, Schoen I. 2021. Site-specifically-labeled antibodies for super-resolution microscopy reveal in situ linkage errors. *ACS Nano* **15**:12161–12170. DOI: <https://doi.org/10.1021/acsnano.1c03677>, PMID: 34184536
- Fulterer A**, Andlauer TFM, Ender A, Maglione M, Eyring K, Woitkuhn J, Lehmann M, Matkovic-Rachid T, Geiger JRP, Walter AM, Nagel KI, Sigrist SJ. 2018. Active zone scaffold protein ratios tune functional diversity across brain synapses. *Cell Reports* **23**:1259–1274. DOI: <https://doi.org/10.1016/j.celrep.2018.03.126>, PMID: 29719243
- Genç Ö**, Davis GW. 2019. Target-wide induction and synapse type-specific robustness of presynaptic homeostasis. *Current Biology* **29**:3863–3873. DOI: <https://doi.org/10.1016/j.cub.2019.09.036>, PMID: 31708391
- Ghelani T**, Escher M, Thomas U, Esch K, Lützkendorf J, Depner H, Maglione M, Parutto P, Gratz S, Matkovic-Rachid T, Ryglewski S, Walter AM, Holcman D, O'Connor Giles K, Heine M, Sigrist SJ. 2023. Interactive nanocluster compaction of the ELKS scaffold and Cacophony Ca^{2+} channels drives sustained active zone potentiation. *Science Advances* **9**:eade7804. DOI: <https://doi.org/10.1126/sciadv.ade7804>, PMID: 36800417
- Gratz SJ**, Ukken FP, Rubinstein CD, Thiede G, Donohue LK, Cummings AM, O'Connor-Giles KM. 2014. Highly specific and efficient CRISPR/Cas9-catalyzed homology-directed repair in *Drosophila*. *Genetics* **196**:961–971. DOI: <https://doi.org/10.1534/genetics.113.160713>, PMID: 24478335
- Gratz SJ**, Goel P, Bruckner JJ, Hernandez RX, Khateeb K, Macleod GT, Dickman D, O'Connor-Giles KM. 2019. Endogenous tagging reveals differential regulation of Ca^{2+} channels at single active zones during presynaptic homeostatic potentiation and depression. *The Journal of Neuroscience* **39**:2416–2429. DOI: <https://doi.org/10.1523/JNEUROSCI.3068-18.2019>, PMID: 30692227
- Grimm JB**, English BP, Chen J, Slaughter JP, Zhang Z, Revyakin A, Patel R, Macklin JJ, Normanno D, Singer RH, Lionnet T, Lavis LD. 2015. A general method to improve fluorophores for live-cell and single-molecule microscopy. *Nature Methods* **12**:244–250. DOI: <https://doi.org/10.1038/nmeth.3256>, PMID: 25599551
- Guerrero G**, Reiff DF, Agarwal G, Ball RW, Borst A, Goodman CS, Isacoff EY. 2005. Heterogeneity in synaptic transmission along a *Drosophila* larval motor axon. *Nature Neuroscience* **8**:1188–1196. DOI: <https://doi.org/10.1038/nn1526>, PMID: 16116446

- Hallermann S, Kittel RJ, Wichmann C, Weyhersmüller A, Fouquet W, Mertel S, Oswald D, Eimer S, Depner H, Schwärzel M, Sigrist SJ, Heckmann M. 2010. Naked dense bodies provoke depression. *The Journal of Neuroscience* **30**:14340–14345. DOI: <https://doi.org/10.1523/JNEUROSCI.2495-10.2010>, PMID: 20980589
- Hatt H, Smith DO. 1976. Non-uniform probabilities of quantal release at the crayfish neuromuscular junction. *The Journal of Physiology* **259**:395–404. DOI: <https://doi.org/10.1113/jphysiol.1976.sp011472>, PMID: 8636
- He Y, Dupree J, Wang J, Sandoval J, Li J, Liu H, Shi Y, Nave KA, Casaccia-Bonnel P. 2007. Crucial role of *Drosophila* neurexin in proper active zone apposition to postsynaptic densities, synaptic growth, and synaptic transmission. *Neuron* **55**:217–230. DOI: <https://doi.org/10.1016/j.neuron.2007.06.029>, PMID: 17640524
- He K, Han Y, Li X, Hernandez RX, Riboul DV, Feghhi T, Justs KA, Mahneva O, Perry S, Macleod GT, Dickman D. 2023. Physiologic and nanoscale distinctions define glutamatergic synapses in tonic vs phasic neurons. *The Journal of Neuroscience* **43**:4598–4611. DOI: <https://doi.org/10.1523/JNEUROSCI.0046-23.2023>, PMID: 37221096
- Heinrich L, Ryglewski S. 2020. Different functions of two putative *Drosophila* $\alpha_2\delta$ subunits in the same identified motoneurons. *Scientific Reports* **10**:13670. DOI: <https://doi.org/10.1038/s41598-020-69748-8>, PMID: 32792569
- Held RG, Liu C, Kaeser PS. 2016. ELKS controls the pool of readily releasable vesicles at excitatory synapses through its N-terminal coiled-coil domains. *eLife* **5**:e14862. DOI: <https://doi.org/10.7554/eLife.14862>, PMID: 27253063
- Holderith N, Lorincz A, Katona G, Rózsa B, Kulik A, Watanabe M, Nusser Z. 2012. Release probability of hippocampal glutamatergic terminals scales with the size of the active zone. *Nature Neuroscience* **15**:988–997. DOI: <https://doi.org/10.1038/nn.3137>, PMID: 22683683
- Hoover KM, Gratz SJ, Qi N, Herrmann KA, Liu Y, Perry-Richardson JJ, Vanderzalm PJ, O'Connor-Giles KM, Broihier HT. 2019. The calcium channel subunit $\alpha_2\delta$ -3 organizes synapses via an activity-dependent and autocrine BMP signaling pathway. *Nature Communications* **10**:5575. DOI: <https://doi.org/10.1038/s41467-019-13165-7>, PMID: 31811118
- Hoppa MB, Lana B, Margas W, Dolphin AC, Ryan TA. 2012. $\alpha_2\delta$ expression sets presynaptic calcium channel abundance and release probability. *Nature* **486**:122–125. DOI: <https://doi.org/10.1038/nature11033>, PMID: 22678293
- Horn C, Offen N, Nystedt S, Häcker U, Wimmer EA. 2003. piggyBac-based insertional mutagenesis and enhancer detection as a tool for functional insect genomics. *Genetics* **163**:647–661. DOI: <https://doi.org/10.1093/genetics/163.2.647>, PMID: 12618403
- James TD, Zwiefelhofer DJ, Frank CA. 2019. Maintenance of homeostatic plasticity at the *Drosophila* neuromuscular synapse requires continuous IP(3)-directed signaling. *eLife* **8**:e39643. DOI: <https://doi.org/10.7554/eLife.39643>
- Jetti SK, Crane AB, Akbergenova Y, Aponte-Santiago NA, Cunningham KL, Whittaker CA, Littleton JT. 2023. Molecular logic of synaptic diversity between *Drosophila* tonic and phasic motoneurons. *Neuron* **111**:3554–3569. DOI: <https://doi.org/10.1016/j.neuron.2023.07.019>, PMID: 37611584
- Kanamori T, Kanai MI, Dairyo Y, Yasunaga K, Morikawa RK, Emoto K. 2013. Compartmentalized calcium transients trigger dendrite pruning in *Drosophila* sensory neurons. *Science* **340**:1475–1478. DOI: <https://doi.org/10.1126/science.1234879>, PMID: 23722427
- Kawasaki F, Felling R, Ordway RW. 2000. A temperature-sensitive paralytic mutant defines a primary synaptic calcium channel in *Drosophila*. *The Journal of Neuroscience* **20**:4885–4889. DOI: <https://doi.org/10.1523/JNEUROSCI.20-13-04885.2000>, PMID: 10864946
- Kittel RJ, Wichmann C, Rasse TM, Fouquet W, Schmidt M, Schmid A, Wagh DA, Pawlu C, Kellner RR, Willig KI, Hell SW, Buchner E, Heckmann M, Sigrist SJ. 2006. Bruchpilot promotes active zone assembly, Ca²⁺ channel clustering, and vesicle release. *Science* **312**:1051–1054. DOI: <https://doi.org/10.1126/science.1126308>, PMID: 16614170
- Kurdyak P, Atwood HL, Stewart BA, Wu CF. 1994. Differential physiology and morphology of motor axons to ventral longitudinal muscles in larval *Drosophila*. *The Journal of Comparative Neurology* **350**:463–472. DOI: <https://doi.org/10.1002/cne.903500310>, PMID: 7884051
- Kurshan PT, Oztan A, Schwarz TL. 2009. Presynaptic $\alpha_2\delta$ -3 is required for synaptic morphogenesis independent of its Ca²⁺-channel functions. *Nature Neuroscience* **12**:1415–1423. DOI: <https://doi.org/10.1038/nn.2417>, PMID: 19820706
- Laghaei R, Ma J, Tarr TB, Homan AE, Kelly L, Tilwawala MS, Vuocolo BS, Rajasekaran HP, Meriney SD, Dittrich M. 2018. Transmitter release site organization can predict synaptic function at the neuromuscular junction. *Journal of Neurophysiology* **119**:1340–1355. DOI: <https://doi.org/10.1152/jn.00168.2017>, PMID: 29357458
- Li X, Goel P, Wondolowski J, Paluch J, Dickman D. 2018. A glutamate homeostat controls the presynaptic inhibition of neurotransmitter release. *Cell Reports* **23**:1716–1727. DOI: <https://doi.org/10.1016/j.celrep.2018.03.130>, PMID: 29742428
- Lipscombe D, Andrade A, Allen SE. 2013. Alternative splicing: functional diversity among voltage-gated calcium channels and behavioral consequences. *Biochimica et Biophysica Acta* **1828**:1522–1529. DOI: <https://doi.org/10.1016/j.bbamem.2012.09.018>, PMID: 23022282
- Lipscombe D, Lopez Soto EJ. 2019. Alternative splicing of neuronal genes: new mechanisms and new therapies. *Current Opinion in Neurobiology* **57**:26–31. DOI: <https://doi.org/10.1016/j.conb.2018.12.013>, PMID: 30703685
- Littleton JT, Ganetzky B. 2000. Ion channels and synaptic organization. *Neuron* **26**:35–43. DOI: [https://doi.org/10.1016/S0896-6273\(00\)81135-6](https://doi.org/10.1016/S0896-6273(00)81135-6)
- Liu KSY, Siebert M, Mertel S, Knoche E, Wegener S, Wichmann C, Matkovic T, Muhammad K, Depner H, Mettke C, Bückers J, Hell SW, Müller M, Davis GW, Schmitz D, Sigrist SJ. 2011. RIM-binding protein, a central

- part of the active zone, is essential for neurotransmitter release. *Science* **334**:1565–1569. DOI: <https://doi.org/10.1126/science.1212991>, PMID: 22174254
- Liu C**, Bickford LS, Held RG, Nyitrai H, Südhof TC, Kaeser PS. 2014. The active zone protein family ELKS supports Ca²⁺ influx at nerve terminals of inhibitory hippocampal neurons. *The Journal of Neuroscience* **34**:12289–12303. DOI: <https://doi.org/10.1523/JNEUROSCI.0999-14.2014>, PMID: 25209271
- Liu S**, Hoess P, Ries J. 2022. Super-resolution microscopy for structural cell biology. *Annual Review of Biophysics* **51**:301–326. DOI: <https://doi.org/10.1146/annurev-biophys-102521-112912>, PMID: 35119945
- Lnenicka GA**, Keshishian H. 2000. Identified motor terminals in *Drosophila* larvae show distinct differences in morphology and physiology. *Journal of Neurobiology* **43**:186–197 PMID: 10770847.
- Los GV**, Encell LP, McDougall MG, Hartzell DD, Karassina N, Zimprich C, Wood MG, Learish R, Ohana RF, Urh M, Simpson D, Mendez J, Zimmerman K, Otto P, Vidugiris G, Zhu J, Darzins A, Klaubert DH, Bulleit RF, Wood KV. 2008. HaloTag: a novel protein labeling technology for cell imaging and protein analysis. *ACS Chemical Biology* **3**:373–382. DOI: <https://doi.org/10.1021/cb800025k>, PMID: 18533659
- Lu Z**, Chouhan AK, Borycz JA, Lu Z, Rossano AJ, Brain KL, Zhou Y, Meinertzhagen IA, Macleod GT. 2016. High-probability neurotransmitter release sites represent an energy-efficient design. *Current Biology* **26**:2562–2571. DOI: <https://doi.org/10.1016/j.cub.2016.07.032>
- Ly CV**, Yao C-K, Verstreken P, Ohyama T, Bellen HJ. 2008. straightjacket is required for the synaptic stabilization of cacophony, a voltage-gated calcium channel alpha1 subunit. *The Journal of Cell Biology* **181**:157–170. DOI: <https://doi.org/10.1083/jcb.200712152>, PMID: 18391507
- Macleod GT**, Chen L, Karunanithi S, Peloquin JB, Atwood HL, McRory JE, Zamponi GW, Charlton MP. 2006. The *Drosophila* cacts2 mutation reduces presynaptic Ca²⁺ entry and defines an important element in Cav2.1 channel inactivation. *The European Journal of Neuroscience* **23**:3230–3244. DOI: <https://doi.org/10.1111/j.1460-9568.2006.04873.x>, PMID: 16820014
- McDonald NA**, Fetter RD, Shen K. 2020. Assembly of synaptic active zones requires phase separation of scaffold molecules. *Nature* **588**:454–458. DOI: <https://doi.org/10.1038/s41586-020-2942-0>, PMID: 33208945
- Medeiros AT**, O'Connor-Giles K. 2023. To Ib or not to b: Transcriptional regulation of tonic type Ib vs. phasic type Is motor neurons. *Neuron* **111**:3497–3499. DOI: <https://doi.org/10.1016/j.neuron.2023.10.033>, PMID: 37972561
- Melom JE**, Akbergenova Y, Gavornik JP, Littleton JT. 2013. Spontaneous and evoked release are independently regulated at individual active zones. *The Journal of Neuroscience* **33**:17253–17263. DOI: <https://doi.org/10.1523/JNEUROSCI.3334-13.2013>, PMID: 24174659
- Miki T**, Kaufmann WA, Malagon G, Gomez L, Tabuchi K, Watanabe M, Shigemoto R, Marty A. 2017. Numbers of presynaptic Ca²⁺ channel clusters match those of functionally defined vesicular docking sites in single central synapses. *PNAS* **114**:E5246–E5255. DOI: <https://doi.org/10.1073/pnas.1704470114>, PMID: 28607047
- Mrestani A**, Pauli M, Kollmannsberger P, Repp F, Kittel RJ, Eilers J, Doose S, Sauer M, Sirén A-L, Heckmann M, Paul MM. 2021. Active zone compaction correlates with presynaptic homeostatic potentiation. *Cell Reports* **37**:109770. DOI: <https://doi.org/10.1016/j.celrep.2021.109770>, PMID: 34610300
- Msghina M**, Millar AG, Charlton MP, Govind CK, Atwood HL. 1999. Calcium entry related to active zones and differences in transmitter release at phasic and tonic synapses. *The Journal of Neuroscience* **19**:8419–8434. DOI: <https://doi.org/10.1523/JNEUROSCI.19-19-08419.1999>, PMID: 10493743
- Muhammad K**, Reddy-Alla S, Driller JH, Schreiner D, Rey U, Böhme MA, Hollmann C, Ramesh N, Depner H, Lützkendorf J, Matkovic T, Götz T, Bergeron DD, Schmoranzler J, Goettfert F, Holt M, Wahl MC, Hell SW, Scheiffele P, Walter AM, et al. 2015. Presynaptic spinophilin tunes neurexin signalling to control active zone architecture and function. *Nature Communications* **6**:8362. DOI: <https://doi.org/10.1038/ncomms9362>, PMID: 26471740
- Müller CS**, Haupt A, Bildl W, Schindler J, Knaus H-G, Meissner M, Rammner B, Striessnig J, Flockerzi V, Fakler B, Schulte U. 2010. Quantitative proteomics of the Cav2 channel nano-environments in the mammalian brain. *PNAS* **107**:14950–14957. DOI: <https://doi.org/10.1073/pnas.1005940107>, PMID: 20668236
- Nakamura Y**, Harada H, Kamasawa N, Matsui K, Rothman JS, Shigemoto R, Silver RA, DiGregorio DA, Takahashi T. 2015. Nanoscale distribution of presynaptic Ca(2+) channels and its impact on vesicular release during development. *Neuron* **85**:145–158. DOI: <https://doi.org/10.1016/j.neuron.2014.11.019>, PMID: 25533484
- Newman ZL**, Hoagland A, Aghi K, Worden K, Levy SL, Son JH, Lee LP, Isacoff EY. 2017. Input-specific plasticity and homeostasis at the *Drosophila* larval neuromuscular junction. *Neuron* **93**:1388–1404. DOI: <https://doi.org/10.1016/j.neuron.2017.02.028>, PMID: 28285823
- Newman ZL**, Bakshinskaya D, Schultz R, Kenny SJ, Moon S, Aghi K, Stanley C, Marnani N, Li R, Bleier J, Xu K, Isacoff EY. 2022. Determinants of synapse diversity revealed by super-resolution quantal transmission and active zone imaging. *Nature Communications* **13**:229. DOI: <https://doi.org/10.1038/s41467-021-27815-2>, PMID: 35017509
- Oh KH**, Xiong A, Choe J-Y, Richmond JE, Kim H. 2023. Active zone trafficking of Cav2/UNC-2 channels is independent of β/CCB-1 and α2δ/UNC-36 Subunits. *The Journal of Neuroscience* **43**:5142–5157. DOI: <https://doi.org/10.1523/JNEUROSCI.2264-22.2023>, PMID: 37160370
- Öztürk-Çolak A**, Marygold SJ, Antonazzo G, Attrill H, Goutte-Gattat D, Jenkins VK, Matthews BB, Millburn G, Dos Santos G, Tabone CJ, FlyBase Consortium. 2024. FlyBase: updates to the *Drosophila* genes and genomes database. *Genetics* **227**:iyad211. DOI: <https://doi.org/10.1093/genetics/iyad211>, PMID: 38301657

- Paez-Segala MG**, Sun MG, Shtengel G, Viswanathan S, Baird MA, Macklin JJ, Patel R, Allen JR, Howe ES, Piszczek G, Hess HF, Davidson MW, Wang Y, Looger LL. 2015. Fixation-resistant photoactivatable fluorescent proteins for CLEM. *Nature Methods* **12**:215–218. DOI: <https://doi.org/10.1038/nmeth.3225>, PMID: 25581799
- Peled ES**, Isacoff EY. 2011. Optical quantal analysis of synaptic transmission in wild-type and rab3-mutant *Drosophila* motor axons. *Nature Neuroscience* **14**:519–526. DOI: <https://doi.org/10.1038/nn.2767>, PMID: 21378971
- Peled ES**, Newman ZL, Isacoff EY. 2014. Evoked and spontaneous transmission favored by distinct sets of synapses. *Current Biology* **24**:484–493. DOI: <https://doi.org/10.1016/j.cub.2014.01.022>, PMID: 24560571
- Peng IF**, Wu CF. 2007. *Drosophila* cacophony channels: a major mediator of neuronal Ca²⁺ currents and a trigger for K⁺ channel homeostatic regulation. *The Journal of Neuroscience* **27**:1072–1081. DOI: <https://doi.org/10.1523/JNEUROSCI.4746-06.2007>, PMID: 17267561
- Petersen SA**, Fetter RD, Noordermeer JN, Goodman CS, DiAntonio A. 1997. Genetic analysis of glutamate receptors in *Drosophila* reveals a retrograde signal regulating presynaptic transmitter release. *Neuron* **19**:1237–1248. DOI: [https://doi.org/10.1016/s0896-6273\(00\)80415-8](https://doi.org/10.1016/s0896-6273(00)80415-8), PMID: 9427247
- Radulovic T**, Dong W, Goral RO, Thomas CI, Veeraraghavan P, Montesinos MS, Guerrero-Given D, Goff K, Lübbert M, Kamasawa N, Ohtsuka T, Young SM Jr. 2020. Presynaptic development is controlled by the core active zone proteins CAST/ELKS. *The Journal of Physiology* **598**:2431–2452. DOI: <https://doi.org/10.1113/JP279736>, PMID: 32304329
- Rebola N**, Reva M, Kirizs T, Szoboszlai M, Lőrincz A, Moneron G, Nusser Z, DiGregorio DA. 2019. Distinct nanoscale calcium channel and synaptic vesicle topographies contribute to the diversity of synaptic function. *Neuron* **104**:693–710. DOI: <https://doi.org/10.1016/j.neuron.2019.08.014>, PMID: 31558350
- Reddy-Alla S**, Böhme MA, Reynolds E, Beis C, Grasskamp AT, Mampell MM, Maglione M, Jusyte M, Rey U, Babikir H, McCarthy AW, Quentin C, Matkovic T, Bergeron DD, Mushtaq Z, Göttfert F, Oswald D, Mielke T, Hell SW, Sigrist SJ, et al. 2017. Stable Positioning of Unc13 restricts synaptic vesicle fusion to defined release sites to promote synchronous neurotransmission. *Neuron* **95**:1350–1364. DOI: <https://doi.org/10.1016/j.neuron.2017.08.016>, PMID: 28867551
- Reuveny A**, Shnyder M, Lorber D, Wang S, Volk T. 2018. Ma2/d promotes myonuclear positioning and association with the sarcoplasmic reticulum. *Development* **145**:dev159558. DOI: <https://doi.org/10.1242/dev.159558>
- Risher WC**, Kim N, Koh S, Choi J-E, Mitev P, Spence EF, Pilaz L-J, Wang D, Feng G, Silver DL, Soderling SH, Yin HH, Eroglu C. 2018. Thrombospondin receptor $\alpha 2\delta$ -1 promotes synaptogenesis and spinogenesis via postsynaptic Rac1. *The Journal of Cell Biology* **217**:3747–3765. DOI: <https://doi.org/10.1083/jcb.201802057>, PMID: 30054448
- Sauvola CW**, Akbergenova Y, Cunningham KL, Aponte-Santiago NA, Littleton JT. 2021. The decoy SNARE Tomosyn sets tonic versus phasic release properties and is required for homeostatic synaptic plasticity. *eLife* **10**:e72841. DOI: <https://doi.org/10.7554/eLife.72841>, PMID: 34713802
- Schöpf CL**, Ablinger C, Geisler SM, Stanika RI, Campiglio M, Kaufmann WA, Nimmervoll B, Schlick B, Brockhaus J, Missler M, Shigemoto R, Obermair GJ. 2021. Presynaptic $\alpha 2\delta$ subunits are key organizers of glutamatergic synapses. *PNAS* **118**:e1920827118. DOI: <https://doi.org/10.1073/pnas.1920827118>, PMID: 33782113
- Sheng J**, He L, Zheng H, Xue L, Luo F, Shin W, Sun T, Kuner T, Yue DT, Wu L-G. 2012. Calcium-channel number critically influences synaptic strength and plasticity at the active zone. *Nature Neuroscience* **15**:998–1006. DOI: <https://doi.org/10.1038/nn.3129>, PMID: 22683682
- Smith LA**, Wang X, Peixoto AA, Neumann EK, Hall LM, Hall JC. 1996. A *Drosophila* calcium channel $\alpha 1$ subunit gene maps to A genetic locus associated with behavioral and visual defects. *The Journal of Neuroscience* **16**:7868–7879. DOI: <https://doi.org/10.1523/JNEUROSCI.16-24-07868.1996>, PMID: 8987815
- Thomas GD**. 2000. Effect of dose, molecular size, and binding affinity on uptake of antibodies. *Methods in Molecular Medicine* **25**:115–132. DOI: <https://doi.org/10.1385/1-59259-075-6:115>, PMID: 21318844
- Tong X-J**, López-Soto EJ, Li L, Liu H, Nedelcu D, Lipscombe D, Hu Z, Kaplan JM. 2017. Retrograde synaptic inhibition is mediated by α -neurexin binding to the $\alpha 2\delta$ Subunits of N-type calcium channels. *Neuron* **95**:326–340. DOI: <https://doi.org/10.1016/j.neuron.2017.06.018>, PMID: 28669545
- Voigt A**, Freund R, Heck J, Missler M, Obermair GJ, Thomas U, Heine M. 2016. Dynamic association of calcium channel subunits at the cellular membrane. *Neurophotonics* **3**:041809. DOI: <https://doi.org/10.1117/1.NPh.3.4.041809>, PMID: 27872869
- Wang LY**, Augustine GJ. 2014. Presynaptic nanodomains: a tale of two synapses. *Frontiers in Cellular Neuroscience* **8**:455. DOI: <https://doi.org/10.3389/fncel.2014.00455>, PMID: 25674049
- Wang T**, Jones RT, Whippen JM, Davis GW. 2016. $\alpha 2\delta$ -3 is required for rapid transsynaptic homeostatic signaling. *Cell Reports* **16**:2875–2888. DOI: <https://doi.org/10.1016/j.celrep.2016.08.030>, PMID: 27626659
- Weiss N**, Zamponi GW. 2017. Trafficking of neuronal calcium channels. *Neuronal Signaling* **1**:S20160003. DOI: <https://doi.org/10.1042/NS20160003>, PMID: 32714572
- Weyhersmüller A**, Hallermann S, Wagner N, Eilers J. 2011. Rapid active zone remodeling during synaptic plasticity. *The Journal of Neuroscience* **31**:6041–6052. DOI: <https://doi.org/10.1523/JNEUROSCI.6698-10.2011>, PMID: 21508229
- Yazaki J**, Kawashima Y, Ogawa T, Kobayashi A, Okoshi M, Watanabe T, Yoshida S, Kii I, Egami S, Amagai M, Hosoya T, Shiroguchi K, Ohara O. 2020. HaloTag-based conjugation of proteins to barcoding-oligonucleotides. *Nucleic Acids Research* **48**:e8. DOI: <https://doi.org/10.1093/nar/gkz1086>, PMID: 31752022

Zhang Y, Wang T, Cai Y, Cui T, Kuah M, Vicini S, Wang T. 2023. Role of $\alpha 2\delta$ -3 in regulating calcium channel localization at presynaptic active zones during homeostatic plasticity. *Frontiers in Molecular Neuroscience* **16**:1253669. DOI: <https://doi.org/10.3389/fnmol.2023.1253669>, PMID: 38025261